ACS Catalysis

pubs.acs.org/acscatalysis

Research Article

Insights into the Mechanism and Reactivity of Zeolite-Catalyzed Alkylphenol Dealkylation

Massimo Bocus and Veronique Van Speybroeck*

Cite This: *ACS Catal.* 2022, 12, 14227−14242

Read Online

ACCESS | Metrics & More | Article Recommendations | Supporting Information

ABSTRACT: In the stride toward the production of low-carbon-footprint commodity chemicals, the development of a complete wood biorefinery plays a pivotal role. The lignin fraction of wood can be depolymerized and demethoxylated mainly into 4-alkylphenols. These phenolic compounds can further catalytically be C-dealkylated within the H-ZSM-5 zeolite at relatively high temperatures and in the presence of steam, producing phenol and olefins. Experimentally, the dealkylation reaction was found to have two striking features: first, different reactants possess very different reactivity. 4-Ethylphenol (4-EP) is somehow less reactive than 4-*n*-propylphenol (4-*n*-PP), which is in turn much less reactive than 4-isopropylphenol (4-*iso*-PP). Second, cofeeding of steam in the reaction mixture was necessary to prevent rapid and reversible catalyst deactivation. Herein, a combination of static and dynamic density functional theory (DFT) simulations is used to unravel the molecular and mechanistic origin of these observations. Free-energy profiles obtained from static calculations confirm the experimentally observed reactivity sequence, where our computations show that the secondary nature of the alkyl carbon involved in 4-*iso*-PP dealkylation strongly stabilizes the respective transition states. To investigate the effect of water on the mobility of the reactive species and their interaction with the active site, we investigated the diffusion of phenol along the H-ZSM-5 straight channel in the presence of water loadings from 0 to 3 molecules per zeolite unit cell. We show that water has a strongly beneficial effect in promoting desorption and diffusion of phenol away from the Brønsted acid site through competitive adsorption and by the formation of hydrogen bond chains with the diffusing phenol. This effect could lead to a shorter residence time inside the zeolite, preventing active site poisoning and condensation to bulkier biphenylether moieties.

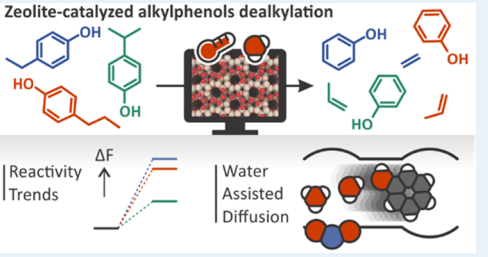

KEYWORDS: *zeolite, DFT, enhanced sampling, dealkylation, water, molecular dynamics, lignin valorization*

1. INTRODUCTION

The depletion of easily accessible crude oil reservoirs around the world, joined with the increasing levels of anthropogenic CO_2 in the atmosphere, is exacerbating the need for new and renewable sources of carbon-based commodity chemicals.[1,2] Being the core of many polymeric materials, aromatics are indispensable for the chemical industries but are nowadays almost exclusively obtained from fossil resources.[3] The identification of sustainable and aromatic-rich raw materials is therefore crucial.

Among all natural polymers, lignin is likely to become such a source of aromatics. Together with (hemi)cellulose, it is one of the main polymeric components of the plant cell wall, and it is generally discarded or used as a low-value fuel in the paper-production process.[4,5] Nevertheless, it possesses the highest percentage by weight of aromatic units with respect to all other natural polymers. Lignin exploitation has been hampered by its heterogeneity and chemical stability that made it difficult to design a straightforward, selective, and efficient depolymerization process.[6] Despite this, the entirely new concept of lignin-first biorefinery has been developed in the past few years.[7,8] Thanks to advanced catalytic systems, it has become possible to depolymerize lignin directly from the raw biomass without significantly degrading the (hemi)cellulosic fraction in a process called reductive catalytic fractionation (RCF).[9,10] If—for instance—birch wood is used, the product oil contains mainly *para-n*-propyl derivatives of guaiacol and syringol (Figure 1, left)[11,12] that can then be demethoxylated using Ni under hydrogen atmosphere, producing *para*-substituted alkylphenols.[8]

The following step in the path toward the production of commodity chemicals consists of further defunctionalization of alkylphenols to obtain basic building blocks useful for the chemical industry. Recently, highly efficient gas-phase dealkylation of alkylphenols was proposed, catalyzed by acidic zeolites (Figure 1, right).[13−16] Among the many tested aluminosilicates, higher selectivity was achieved with the H-

Received: August 4, 2022
Revised: October 11, 2022

https://doi.org/10.1021/acscatal.2c03844
ACS Catal. 2022, 12, 14227−14242

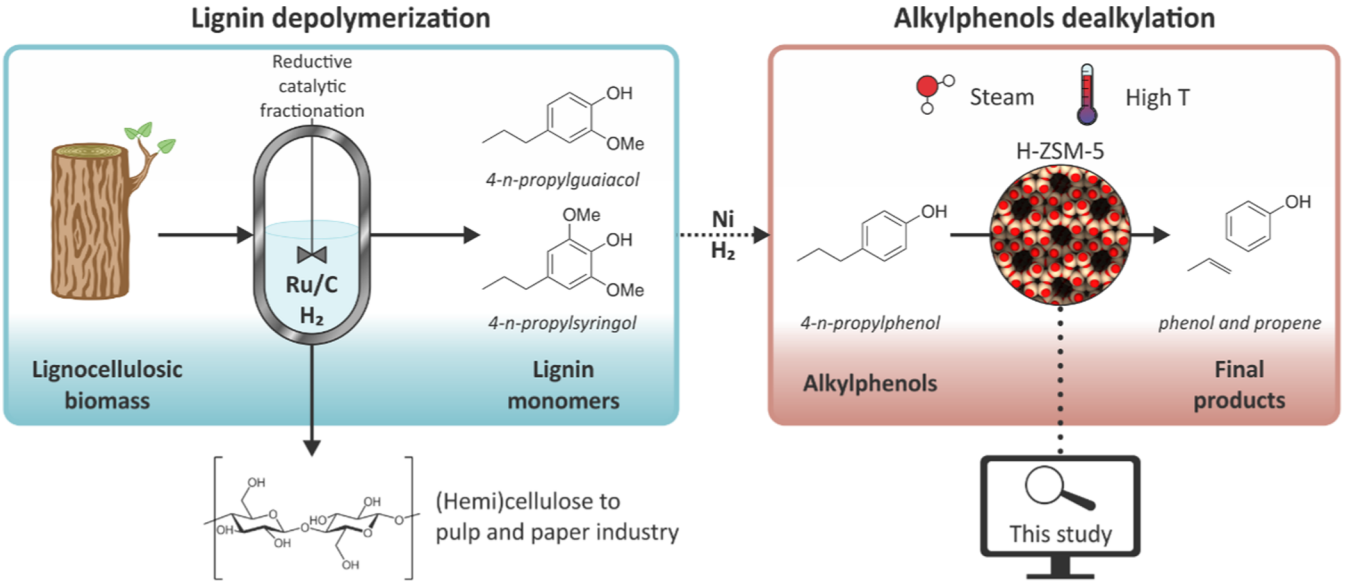

Figure 1. Schematic representation of the lignin-to-chemicals process. The lignocellulosic biomass undergoes reductive catalytic fractionation (RCF, blue box). In the process, lignin is depolymerized in a mixture of lignin monomers, while the (hemi)cellulosic fraction is recovered for further usage. The lignin monomers can be demethoxylated with a Ni catalyst under hydrogen to produce alkylphenols, which are then further dealkylated using the H-ZSM-5 zeolite at high temperatures and in the presence of steam (red box).

ZSM-5 zeolite with a moderately high Si/Al ratio (*vide infra*). It was also found that the presence of steam is important to prevent rapid catalyst deactivation. The reaction requires fairly high temperatures (500−600 K depending on the substrate) for the entropic gain to overcome the positive enthalpic variation.[15] The products, phenol and olefins, are both very valuable and requested by many industrial chemical processes.[8]

When 4-ethylphenol (4-EP), 4-*n*-propylphenol (4-*n*-PP), and 4-isopropylphenol (4-*iso*-PP) are used as model reactants for the dealkylation reaction (Figure 2a), it was experimentally observed that they present very different reactivities.[14,15] Specifically, 4-EP is the less reactive reagent, reaching ∼50% conversion at about 650 K (over H-ZSM-5 with Si/Al = 40). 4-*n*-PP is slightly more reactive, ∼50% of conversion being achieved around 575 K. 4-*iso*-PP, finally, is extremely active and almost full conversion can already be observed below 500 K. The reasons underlying such a large reactivity difference, however, were not fully understood.

A further option in the path toward commodity chemicals that was recently explored consists in avoiding the demethoxylation step and simply demethylate the lignin-derived 4-alkylguaicols.[17] This produces 4-alkylcatechols, that can be dealkylated in a similar fashion as the 4-alkylphenols to produce catechol and olefins. While the presence of the second hydroxyl group leads to a more complex chemistry and lower yields are observed, it does not seem to extensively influence the reactivity toward dealkylation, which is similar between 4-*n*-PP and 4-*n*-PC (4-*n*-propylcatechol).[17]

Another peculiar aspect of the alkylphenol dealkylation reaction, which remarkably differentiates it from dealkylations on purely hydrocarbon substrates, is that steam is required to prevent quick and reversible catalyst deactivation. This was attributed to water preventing the condensation of phenol to diphenylether, by both disfavoring the reaction equilibrium as well as promoting phenol desorption from the zeolite active sites.[15] This effect is very prominent, as Arrhenius activation energies measured for the dealkylation of 4-*n*-PP[15] resulted to be higher in the presence of water (from 67−68 to 99−103 kJ·mol^{-1}) but, on the other hand, the measured dealkylation rate was faster as in the absence of water an almost instantaneous poisoning of the dry catalyst was observed. While the impact of water on intrinsic reactivity is an active field of research,[18−20] its effect on diffusivity of reactive compounds is still relatively unexplored.

Within the field of zeolite catalysis, *ab initio* periodic calculations using density functional theory (DFT) have been extensively used to provide valuable mechanistic insights for a wide range of industrially relevant reactions.[21,22] To the best of our knowledge, the chemistry of alkylphenols in zeolites has not received—from a computational perspective—a large attention so far. The investigations have mostly focused on the alkylation of phenol with alcohols, such as methylation over H-FAU[23] and tert-butylation over H-BEA.[24] On the other hand, a well-characterized reaction is the alkylation of benzene with olefins,[20,25−29] used industrially to produce ethylbenzene. This reaction represents a relevant means of comparison for our case study as it consists in the opposite process with respect to dealkylation. Based on its known mechanistic features, it can be assumed that the dealkylation of alkylphenols can proceed through three possible pathways (Figure 2b): initially, the molecule is protonated at the *para* carbon by the BAS, forming an arenium ion commonly known as Wheland complex (**II**). This intermediate is a key representative of the rich carbocation chemistry within zeolite pores[30,31] and its existence has recently been proven experimentally during benzene ethylation in H-ZSM-5 through UV−vis spectroscopy[32] and by our group through enhanced sampling simulations at operating conditions.[20] Given the higher nucleophilicity of phenol with respect to benzene, the Wheland complex formation should be even more prominent in this case. After protonation, the substrate can then undergo a concerted dealkylation step (TS2 in Figure 2b) to immediately give the final products (**III**). Alternatively, the alkyl group can be transferred to the zeolite framework, forming a surface alkoxide species (SAS, **IV**) that can subsequently deprotonate to give the final alkene. Finally,

https://doi.org/10.1021/acscatal.2c03844
ACS Catal. 2022, 12, 14227−14242

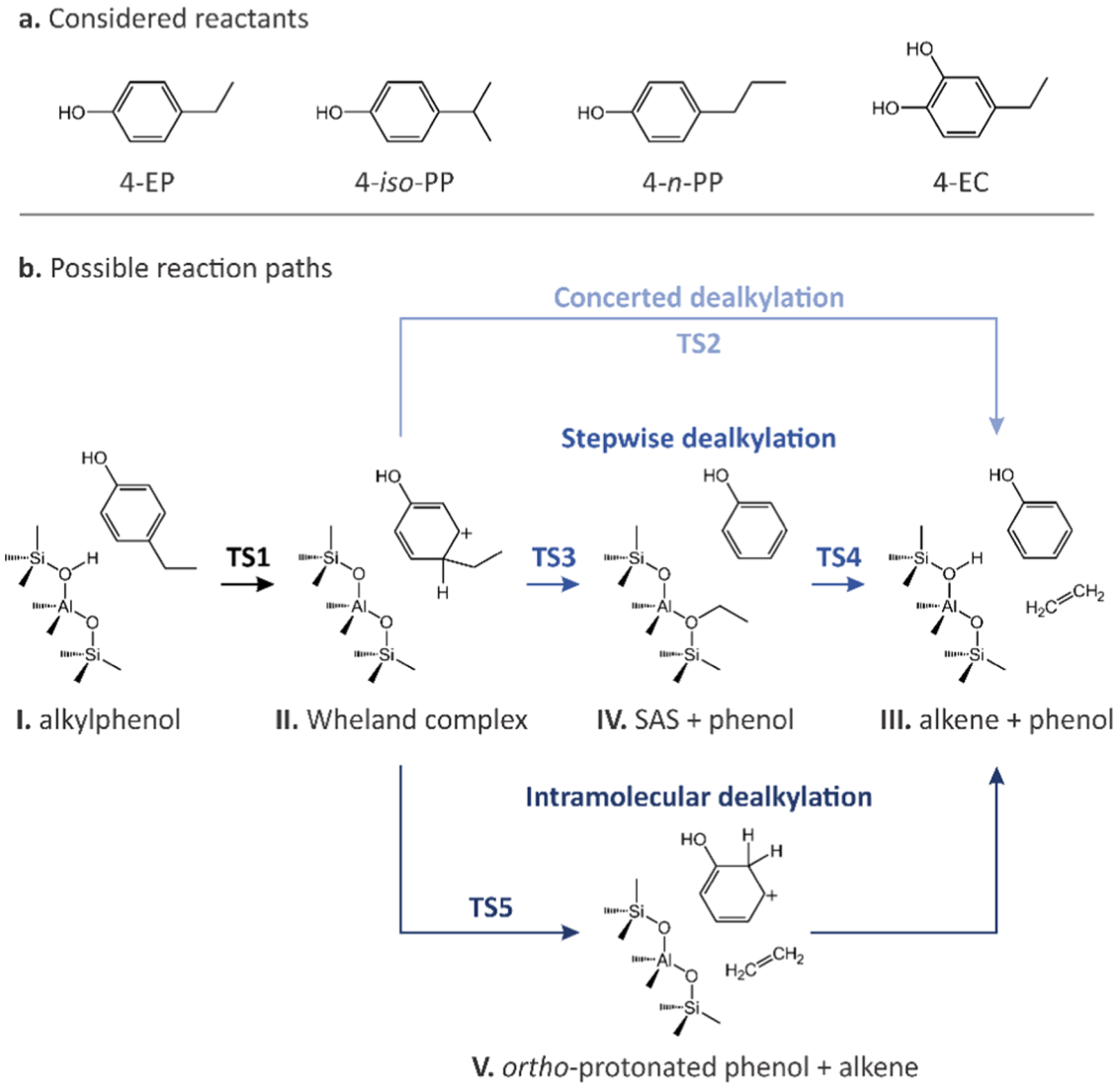

Figure 2. (a) The four reactants considered in this work, namely, 4-ethylphenol (4-EP), 4-*n*-propylphenol (4-*n*-PP), 4-isopropylphenol (4-*iso*-PP), and 4-ethylcatechol (4-EC). (b) Three possible mechanistic pathways for the conversion of an alkylphenol (**I**, 4-EP is used as the model reagent) into phenol and an alkene (**III**) are investigated: they all start with the formation of a Wheland complex (**II**) that can undergo concerted dealkylation (TS2), a stepwise path (TS3, TS4) with the formation of an intermediate surface alkoxide species (SAS, **IV**) or an intramolecular dealkylation (TS5), which leads to *ortho*-protonated phenol (**V**).

inspired by the work of Kolboe et al.,[33] we also investigated an intramolecular dealkylation where the alkyl tail transfers its excess proton to the *ortho* position of the aromatic ring (TS5 and intermediate **V** in Figure 2b). The latter can then transfer a proton back to the zeolite framework to give the final products.

To gain a better understanding of the preferred mechanism and the reactivity differences between various substrates during the H-ZSM-5-catalyzed alkylphenol dealkylation, we thoroughly investigated the behavior and reactivity of 4-EP, 4-*n*-PP, 4-*iso*-PP, and 4-EC (4-ethylcatechol) employing static and dynamic periodic DFT calculations. While the former represents a computationally efficient tool to unravel activation and adsorption energies of reacting species, the latter allows to better explore the flat potential energy surface (PES) in the catalyst pores for highly mobile species, thus better reproducing their behavior at realistic *operando* conditions.[34] We show that the static results allow to rationalize the reactivity differences between the various alkylphenols, with reaction barriers that are in line with the experimental kinetic measurements.

To obtain insight into the effect of water on the adsorption and diffusion of phenolic compounds, umbrella sampling (US) molecular dynamics simulations were performed to study the diffusion of phenol through the zeolite pore system in the anhydrous and hydrated case. Molecular dynamics simulations at operating conditions are quintessential to account for the high mobility of water in the pores of the zeolite. Water is shown to greatly improve the desorption and diffusion of phenol away from the BAS. This is caused by competitive adsorption between water and phenol on the BAS and, at the same time, to the formation of hydrogen bond chains between water and the phenol hydroxyl group when the latter moves away from the active site.

2. COMPUTATIONAL DETAILS

Three main types of periodic DFT calculations have been performed to investigate the reactivity differences between the

https://doi.org/10.1021/acscatal.2c03844
ACS Catal. 2022, 12, 14227−14242

considered alkylphenolic reactants (see Figure 2a) and to assess the impact of water on phenol diffusion. First, regular molecular dynamics (MD) simulations have been used to investigate the behavior of the main possible dealkylation intermediates (Figure 2b) and obtain insights in their stability and behavior at operating conditions. Then, static calculations allowed to compute the free-energy barriers for the whole dealkylation mechanism, providing some interesting reactivity trends, while being significantly less computationally demanding than MD simulations. Finally, to assess the role of water on phenol diffusion, the static approach is insufficient due to the high mobility of the water molecules and their strong interaction with the BAS, which can also result in its complete abstraction from the framework.[20,35,36] On the other hand, the diffusion of aromatics along the H-ZSM-5 straight channels is also an activated process;[37] therefore, it is impossible to sample the diffusion of phenolic compounds during a regular MD simulation. To simulate diffusion of phenol in the presence of water at operating conditions, we have used umbrella sampling molecular dynamics simulations according to a procedure introduced earlier by some of the presenting authors.[38,39]

2.1. Catalyst Model. All simulations are performed in a periodic H-ZSM-5 model, that allows to account for the confinement effects induced by the zeolite three-dimensional pore structure. The H-ZSM-5 zeolite possesses an MFI topology, consisting of straight 10-rings channels intersected by sinusoidal ones. The unit cell contains 96 tetrahedral silicon atoms connected by oxygen bridges. As previously done,[40,41] we substituted the Si at the T12 position with an aluminum atom obtaining a Si/Al ratio of 95. This is comparable with the experimental Si/Al ratio of 40,[15] which should mainly correspond to isolated active sites. The T12 site is located at the channel intersection and it ensures maximal accessibility for the substrate (Figure S1).[42] The negative charge created by the Al substitution is compensated by the addition of a proton on the O_{Z1}, adjacent to the defective site. The unit cell parameters used in the static simulations are analogous to the optimized ones reported in ref 43 (a = 20.02 Å, b = 20.25 Å, c = 13.49 Å, α = 89.87°, β = 89.69°, and γ = 90.10°).

2.2. Static Calculations. All of the computed reaction barriers were obtained by means of static periodic DFT simulations. We used the Vienna *Ab initio* Simulation Package (VASP 5.4.4)[44−46] with the Projected Augmented Wave (PAW) method.[47,48] The Perdew−Burke−Ernzerhof (PBE)[49] exchange-correlation functional coupled with Grimme's D3 dispersion scheme[50] was employed in all calculations. The plane wave energy cutoff was set to 600 eV, while the self-consistent field (SCF) convergence threshold was set to 10^{-5} eV. To ensure that the same truncated basis set is used in all calculations, we fixed the cell volume and parameters at their optimized values (*vide supra*). Because of the large unit cell dimensions, the sampling of the Brillouin zone was restricted to the Γ-point.

The transition states search and optimization was performed using the improved dimer method.[51] Initial guess structures were prepared with the ZEOBUILDER software.[52] The optimized geometries were then further refined using a quasi-Newton algorithm.[53] The reactant and product states for each optimized transition state were generated by slightly displacing the structure along the normal mode with imaginary frequency corresponding to the transition-state crossing and then fully optimized with the conjugate gradient method. In all cases, the geometry optimization was stopped when the energy difference between two subsequent steps was lower than 10^{-4} eV.

Each stationary point was characterized with a normal mode analysis (NMA) in the harmonic approximation. A partial Hessian vibrational analysis (PHVA)[54] was used, including the adsorbed molecules and a T8 cluster around the BAS position. This choice was shown to be sufficient to obtain good results for the calculated thermodynamic properties.[55] A minimum in the potential energy surface (PES) should be characterized exclusively by positive vibrational frequencies, while a transition state by a single imaginary frequency along the reaction coordinate. In some cases, however, the flat PES in the zeolite pores makes it extremely difficult to remove all imaginary modes with very low frequency, even after multiple reoptimizations of the system. Those modes correspond with (almost free) rotations and translations of the adsorbed species in the zeolite pores. We then considered an optimization converged if, after two subsequent reoptimization attempts following the residual undesired imaginary mode(s), the computed energy variation was lower than 1 kJ·mol^{-1}. The remaining imaginary frequencies were replaced with an arbitrary value of 60 cm^{-1}, as proposed by De Moor et al.[55]

The same procedure was performed for other low-frequency modes (below 60 cm^{-1}) similarly to what has already been proposed in the literature, to reduce the numerical uncertainty and their impact on the calculation of the entropy.[56−58] Finally, the normal modes spectrum was used to calculate enthalpy, entropy, and free energy of adsorption for each species at the reaction temperature,[59] as implemented in our in-house-developed software TAMkin.[60]

2.3. Molecular Dynamics Simulations. To study the behavior and stability of adsorbed species in the zeolite fully taking into account their mobility and the flexibility of the catalyst, ab initio molecular dynamics (AIMD) simulations were performed. The CP2K software package (version 5.1)[61,62] was used, combining plane waves with a Gaussian atom-centered basis set (GPW).[63,64] In line with the static calculations, energies and forces were evaluated at a PBE-D3[49,50] level of theory, where we however resort to its revPBE parametrization because of its improved results.[65] A DZVP quality basis set with GTH pseudopotentials[66] was adopted and the plane wave energy cutoff set to 350 Ry. All simulations were performed in the NPT ensemble with a time step for integration of the equation of motion set to 0.5 fs. The temperature was controlled by a chain of five Nosé−Hoover thermostats,[67,68] while the pressure was controlled by an MTK barostat.[69]

2.4. Umbrella Sampling. The effect of water coadsorbed on the active site with phenol in potentially assisting and favoring desorption and diffusion of the latter was probed using umbrella sampling (US) simulations.[70,71] As a model system, a single phenol molecule was placed in proximity of the active site and, for the hydrated cases, one, two, or three additional water molecules were also introduced in its proximity.

In US, a set of quadratic bias potentials (V_i (CV)) defined as

$$V_i(\mathrm{CV}) = \frac{\kappa_i}{2}(\mathrm{CV} - \mathrm{CV}_{0,i})^2 \quad (1)$$

is applied along an *a priori* defined collective variable (CV). Each bias is characterized by a harmonic spring constant κ_i and it is centered at the CV value $CV_{0,i}$. In this case, the CV was chosen to effectively describe the diffusion of phenol along the

https://doi.org/10.1021/acscatal.2c03844
ACS Catal. 2022, 12, 14227−14242

straight channel of H-ZSM-5, moving from the channel intersection with the BAS to the adjacent one, as schematically illustrated in Figure 3. While *ad hoc* CVs have been reported to

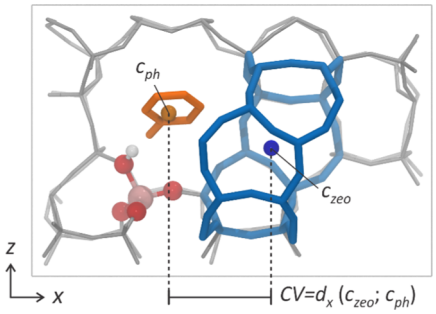

Figure 3. *x* component of the distance between the geometric center (c) of the phenol C and O atoms (in orange) and the geometric center of the double ring separating the two channel intersections in the H-ZSM-5 unit cell (in blue) is chosen as CV to describe the diffusion of phenol along the zeolite straight channel. The location of the Al tetrahedra and the BAS is highlighted in ball-and-stick representation, while the rest of the framework atoms (only half of them is shown) are in gray for the sake of clarity.

study diffusion in other zeolite frameworks,[38,39] we here found that using the *x* component of the distance between the geometric center of the C and O phenol atoms and the geometric center of the skewed double ring that separates two channel intersections in H-ZSM-5 is effective in describing the diffusion process along the straight channel (Figure 3).

A set of 12 umbrellas were used to sample the diffusion from the channel intersection with the BAS (CV ∼ −6 Å) up to CV ∼ 3 Å (being solely interested in the diffusion barrier, the actual diffusion in the second intersection was not considered), whose $CV_{0,i}$ and κ_i parameters are reported in Table S4. These parameters were kept the same independently of the water loading in the unit cell. An AIMD was then performed in each one of the umbrellas. To speed up the simulations, a switch was made to the NVT ensemble, where the average cell lengths of the 653 K MD simulation of 4-EP were used (20.22, 20.40, 13.60 Å). Cell angles were fixed to 90°, as the average values were negligibly different from 90° (<0.1°) and an orthorhombic unit cell symmetry remarkably reduces the computational time in CP2K.

A 100 ps long MD simulation was performed for each umbrella and the first 2.5 ps was excluded as equilibration time. To obtain reliable statistics out of the simulations, it is important that the CV time series are subsampled to decorrelate the datapoints. This was done using the Pymbar library.[72,73] The molecular motion in the zeolite channel is a slow process and, therefore, very high statistical inefficiencies were obtained (∼0.3 ps). Hence the long simulation time per umbrella. The decorrelated time series were then used to obtain the final free-energy profiles (FEPs) through the weighted histogram analysis method (WHAM), as implemented in our in-house-developed ThermoLIB library.[74] Additional benchmark calculations were performed to validate that the resulting FEPs negligibly depend on the plane-waves cutoff (Section S5.2). The error estimate on the FEP was also computed with the ThermoLIB using the Fisher information matrix of the maximum likelihood estimator (MLE).[74] An additional set of US simulations were performed to investigate the impact of water on TS2 for 4-EP, 4-*n*-PP, and 4-*iso*-PP, as in all cases, it was found to be the most favorable dealkylation path (*vide infra*). The related computational details are extensively reported in Section S4.1.

3. RESULTS AND DISCUSSION

3.1. Mobility and Stability of Reaction Intermediates at *Operando* Conditions. As explained in the introduction (Figure 2), various intermediates can be expected to occur in the H-ZSM-5 catalyst during alkylphenols dealkylation. To gain preliminary insights into their behavior and stability at *operando* conditions, AIMD simulations were performed on the reactive alkylphenols, on the *para*-protonated Wheland complexes and on the SAS that can be formed during the dealkylation of 4-EP, 4-*n*-PP, and 4-*iso*-PP. Moreover, alkyl cations corresponding to the protonated product alkenes were also simulated, to understand whether their existence might be possible at relatively high reaction temperatures. Each simulation was carried out for 40 ps at a temperature of 653 K and/or 900 K. The former corresponds to the one at which the least reactive 4-EP reaches full conversion experimentally,[14]

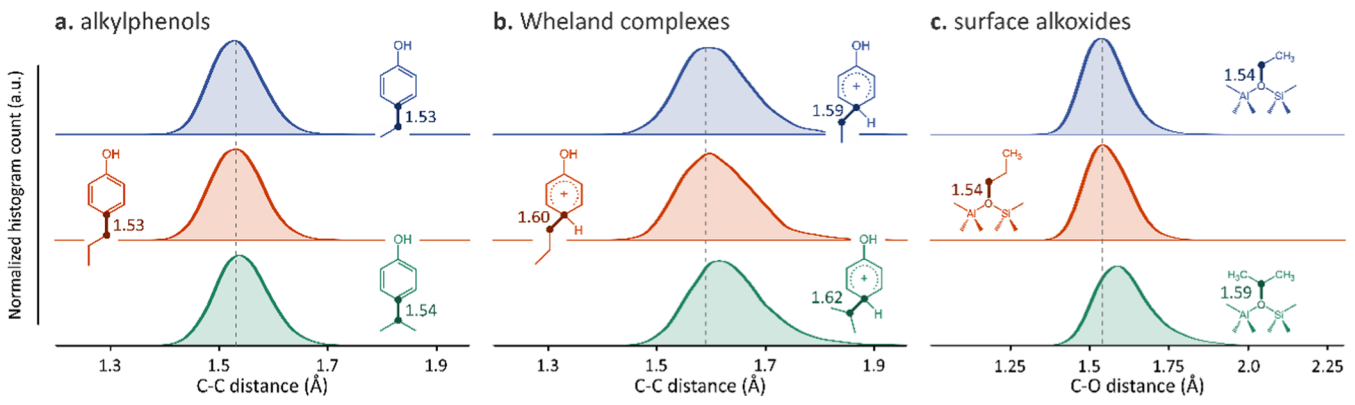

Figure 4. Wheland complex and surface alkoxide intermediates of 4-*iso*-PP present, on average, an elongated reactive bond. This can be seen in the normalized histogram distributions of relevant bond lengths (highlighted with a dark color in the structures drawings) observed in the 653 K MD simulations of (a) neutral alkylphenols, (b) Wheland complexes, and (c) surface alkoxides of 4-EP (blue), 4-*n*-PP (red), and 4-*iso*-PP (green). The dotted gray line is centered at the maximum of the 4-EP distribution and it is only meant to guide the reader's eye. The values reported near the structures drawings are the bond lengths at which the various distributions reach their maximum.

https://doi.org/10.1021/acscatal.2c03844
ACS Catal. 2022, 12, 14227−14242

while the latter was selected to increase the probability of sampling rare events during the simulation time.

3.1.1. 4-Alkylphenols. A single molecule of 4-EP, 4-*n*-PP, or 4-*iso*-PP was introduced in the zeolite channel intersection, close to the BAS location. All of them resulted to be stable during the simulation at 653 K. The observed mobility in the zeolite pore system is low in all cases, as none was able to diffuse away from the channel intersection (see Figure S2). 4-EP and 4-*n*-PP positioned themselves with the alkyl tail aligned along the straight channel. This configuration allows them to strongly interact with the BAS, mainly through a hydrogen bond with their hydroxyl group. Despite such hydrogen bond being the prevalent interaction, the molecules have enough freedom to slightly move back and forth along the straight channel, occasionally exposing the aromatic π cloud to the BAS (Figure S3a,b). The possibility of the molecule to interact with the BAS through the aromatic π cloud is important as the transfer of the BAS proton to the ring represents the initial step of the dealkylation reaction.

4-*iso*-PP behaves quite differently. Its isopropyl tail, indeed, is too hindered to be easily accommodated into the straight channel and pushes the aromatic ring forward (Figure S2c). This prevents the formation of a strong hydrogen bond between the BAS (mainly because of its location in our model) and the OH group of 4-*iso*-PP, with an O···H distance constricted between 2 and 3 Å (Figure S3c). On the other hand, the hindrance of the isopropyl tail has a low impact on the C−C bond involved in the dealkylation reaction, whose length distribution is fundamentally identical to 4-EP and 4-*n*-PP (Figure 4a).

In the 900 K simulations, interestingly, we observed protonations and deprotonations of the aromatic ring for 4-*n*-PP and 4-*iso*-PP (Figure S4). This indicates that the protonation of the aromatic ring is a low-activated process and an equilibrium between protonated and neutral alkylphenols may exist in the confined pores. In both cases, the *ortho* position was protonated. This can be expected as the positive charge in the ring is stabilized by the presence of the hydroxyl group. Moreover, there are two equivalent *ortho* carbon and only one *para* carbon, making the protonation on the former likelier to occur.

3.1.2. Wheland Complexes. For each of the three reactants, the relative *para*-protonated Wheland complexes were simulated, both at high and low temperatures. They are all stable during the whole simulation at a low temperature and, as the neutral reactants, their mobility is limited to the channel intersection. In the high-temperature simulations, 4-EP and 4-*n*-PP remained stable during the whole simulation. For 4-*iso*-PP, we observed proton hopping from the *para* to the *meta* carbon after 35 ps of simulation. The *meta* protonated arenium ion remained stable for 4 ps, after which the proton hopped again back on the *para* carbon. Differently from the simulation of the reactants, no deprotonation/protonation events were observed in this case, which is most likely due to the relatively short simulation times.

By analyzing the C−C bond distance of the 653 K simulations, it is observed that in all of the cases, the average bond length is longer than the neutral reactants, increasing from 1.53−1.54 to 1.59−1.62 Å (Figure 4b). Such an increase is to be expected because of the change in the *para* carbon hybridization. The 4-protonated 4-*iso*-PP has, in this case, a significantly elongated C−C bond than the other two reactants (Figure 4b), pointing toward a higher reactivity of the intermediate.

3.1.3. Surface Alkoxides. Surface alkoxide species were simulated in the presence of a phenol molecule coadsorbed in their proximity, to mimic the dealkylation intermediate **III** (Figure 2b). The differences between the reactive bond lengths become even more accentuated than for the Wheland complexes, with the surface isopropoxide having an average C−O bond length of 1.59 *vs* 1.54 Å for the ethoxide and *n*-propoxide (Figure 4c). The general increase in the analyzed bond lengths for the 4-*iso*-PP intermediates can be attributed to two main effects caused by the double substitution on the central alkyl carbon. First, the two methyl groups produce a larger steric hindrance and, second, the incipient positive charge on the central carbon is stabilized by the inductive effect of two substituents instead of one, as in the case of 4-EP and 4-*n*-PP. Interestingly, during the 900 K simulation of the surface isopropoxide, a complete breaking of the C−O bond was observed after ∼3 ps (Figure S5). The newly formed isopropyl cation remained stable for ∼4 ps, after which a proton was transferred back to the framework, leading to the formation of propene and phenol (Figure S5). This large decrease in the stability of the surface alkoxides based on the number of alkyl substituents on the framework-bounded carbon is in good agreement with the observations made by Cnudde et al. for the intermediates involved in the alkenes cracking reaction[75] and points, again, toward a higher reactivity of the 4-*iso*-PP intermediates.

A similar analysis was performed for the alkyl cations (see Section S2.3), where it was found that they are, in general, not stable. Only the isopropyl cation can survive for a limited amount of time during the molecular dynamics simulations.

In this section, we have analyzed the stability and behavior of the reaction intermediates that might be formed in the H-ZSM-5 zeolite during the dealkylation reaction of 4-EP, 4-*n*-PP, and 4-*iso*-PP. The reactants, 4-protonated Wheland complexes, and surface alkoxides represent minima in the free-energy surface at reaction conditions, thus constituting relevant reaction intermediates. Except for the likely metastability of the isopropyl cation, alkyl cations are not stable and will then not be explicitly considered in our mechanistic investigation. By looking at the bond length distribution of the reactive Wheland complexes and surface alkoxides, it can be seen how the 4-*iso*-PP intermediates present a slightly elongated reactive bond, which is attributed to steric hindrance and inductive stabilization of the incipient positive charge formed on the reactive carbon when the bond is stretched.

3.2. Free-Energy Profile of Alkylphenols Dealkylation from Static Calculations. As shown in the introduction (Figure 2b), three possible mechanisms for the dealkylation of alkylphenols are investigated based on previous studies performed on the alkylation of benzene. To summarize, the aromatic ring of the alkylphenol (**I**) is initially protonated on the *para* position (TS1) to form an intermediate Wheland complex (**II**). This intermediate can undergo a concerted dealkylation (TS2), immediately giving the final phenol and alkene products (**III**). Alternatively, the alkyl group can be transferred to the zeolite framework (TS3) forming a surface alkoxide species (**IV**) which, by concerted scission of the C−O bond and deprotonation (TS4), leads again to the final alkene product. Finally, an intramolecular mechanism is also considered, where a proton of the alkyl tail is transferred to

https://doi.org/10.1021/acscatal.2c03844
ACS Catal. 2022, 12, 14227−14242

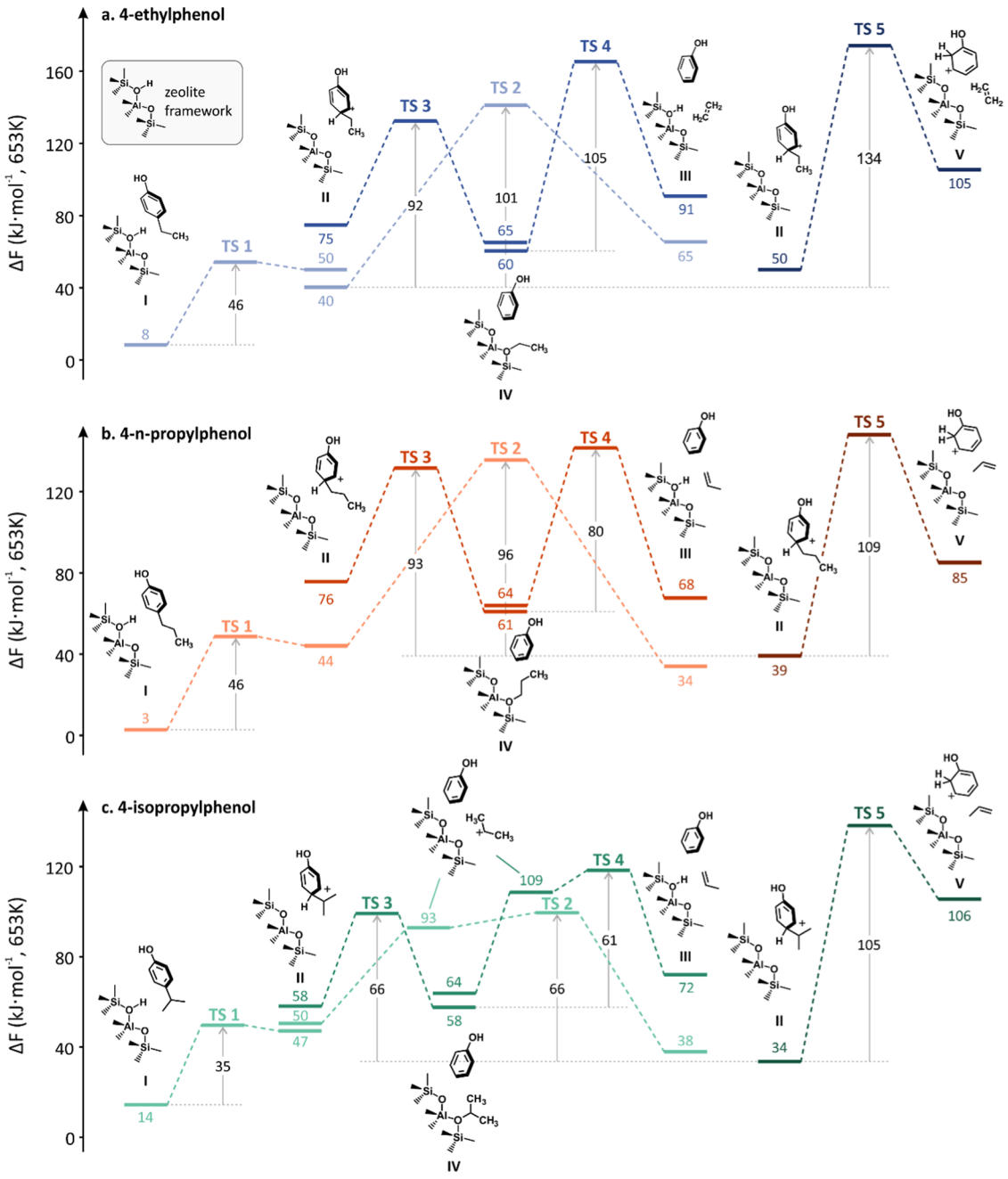

Figure 5. Free-energy profiles (653 K) for all possible dealkylation mechanisms of (a) 4-EP, (b) 4-*n*-PP, and (c) 4-*iso*-PP. The reference value for the free energies corresponds to the empty zeolites and the reacting alkylphenol in gas phase. Activation energies and free energies of the intermediates are reported in kJ·mol^{-1}. For the sake of clarity, TS5 is reported on the right of the profiles, despite its reactant state corresponding to the reactant states of TS2 and TS3.

the *ortho* position of the aromatic ring instead of the zeolite (TS5).

The energetics of all of these transition states were computed through static calculations, as well as the reactants and products connecting them for 4-EP, 4-*n*-PP, and 4-*iso*-PP, as described in Section 2. The free-energy profiles for the three species are shown in Figure 5 and the explicit activation free energies are listed in Table 1. All free-energy values, together with the respective enthalpic and entropic contributions, are listed in Table S2. A graphical visualization of the optimized transition-state geometries is provided in Figure 6.

For all reactants, the protonation of the aromatic ring (TS1) is relatively low activated, with barriers of 46 kJ·mol^{-1} for 4-EP and 4-*n*-PP and 35 kJ·mol^{-1} for 4-*iso*-PP, in good agreement with the observations made from the MD simulations. The Wheland complex was always localized as a stable intermediate; however, its energy can vary substantially, *e.g.*, variations up to 35 kJ·mol^{-1} in the case of 4-EP, depending on its specific orientation in the zeolite framework. Such large dependencies of the computed energies on the orientation of a molecule in the zeolite framework is well-known for static calculations.[58] Here, this difference in orientation originates from the fact that the reactant and product geometries are relaxed directly from the respective transition state, thus ending up in different local minima on the flat potential energy surface of the channel intersection. A clear example is the

https://doi.org/10.1021/acscatal.2c03844
ACS Catal. 2022, 12, 14227−14242

Table 1. Forward ($\Delta F_f^{\ddagger}$) and Backward ($\Delta F_b^{\ddagger}$) Activation Free Energies (kJ·mol^{-1}) for the Various Transition States of the Dealkylation Process, as Obtained from Static Calculations[a]

	TS1		TS2		TS3		TS4		TS5		
reactant	$\Delta F_f^{\ddagger}$	$\Delta F_b^{\ddagger}$	$\Delta F_f^{\ddagger}$	$\Delta F_b^{\ddagger}$	$\Delta F_f^{\ddagger}$	$\Delta F_b^{\ddagger}$	$\Delta F_f^{\ddagger}$	$\Delta F_b^{\ddagger}$	$\Delta F_f^{\ddagger}$	$\Delta F_b^{\ddagger}$	$\Delta F_{tot}^{\ddagger}$
4-EP	46	4	101	76	58	67	105	74	124	69	141
4-*n*-PP	46	4	91	101	56	71	77	74	109	63	135
4-*iso*-PP	35	3	49[b]	62[b]	41	42	54[b]	46[b]	105	33	100
4-EC	56	−2[c]	95	89	47	61			129	70	137

[a] $\Delta F_{tot}^{\ddagger}$ is the overall free-energy barrier to overcome from the reference gas-phase molecules to TS2, which in all cases is the lowest activated. Note that these values refer to the reactant and product states obtained from the TS optimization and, therefore, do not necessarily correspond with the barriers reported in Figures 5 and 7. [b] Referred to the actual reactants, not the metastable isopropyl cation found as intermediate minimum. [c] Artifact due to the frequency calculation (see main text).

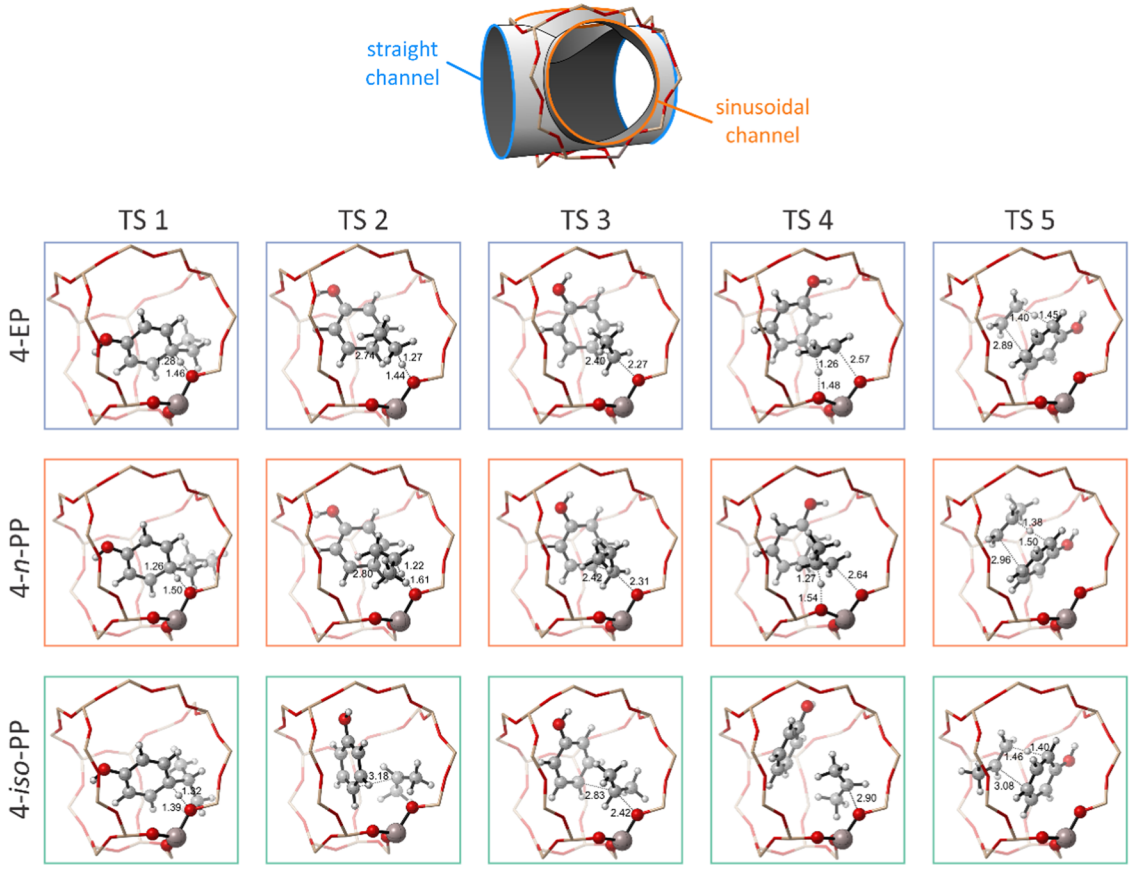

Figure 6. Relaxed transition-state geometries for the dealkylation of 4-EP, 4-*n*-PP, and 4-*iso*-PP. Relevant distances are reported in Å. For the sake of clarity, only the portion of framework surrounding the channel intersection is shown; a schematic representation of the straight and sinusoidal channel orientations is provided in the top figure.

reactant state of TS3 that, in all cases, is higher in energy than the reactant state of TS2 and the product state of TS1. The reason for this is that, to expose the alkyl tail toward the framework, the Wheland complex must rotate producing a hindered configuration where the acidic proton on the *para* carbon is no longer interacting with the oxygens in the first coordination sphere of the Al defect (compare with Figure 6). For the discussion of the reaction barriers hereafter, we systematically used the lowest energetic structure as reference (Figure 5). Furthermore, we opted to consider similar orientations for analogous transition states across the various reactants to allow a systematic comparison between the various alkylphenolic compounds. It can indeed be reasonably assumed that the interconversion between the local minima obtained when optimizing from different transition states is much faster than overcoming the actual reaction barriers.

For the dealkylation of 4-EP (Figure 5a), the concerted dealkylation (TS2) is somehow favorite with respect to the other two investigated mechanisms. With a computed free-energy barrier of 101 kJ·mol^{-1} (referred to as the Wheland complex **II**), the rate is slower than the formation of a surface ethoxide species (SES) in the stepwise mechanism (TS3, 92 kJ·mol^{-1}). However, forming the SES is also an endergonic process (+20 kJ·mol^{-1}) and its subsequent deprotonation (TS4) presents a barrier of 105 kJ·mol^{-1} (referred to as the surface ethoxide intermediate **IV**). Therefore, an overall barrier of 125 kJ·mol^{-1} must be overcome to move from the Wheland complex (**II**) to the products (**III**) through the stepwise path. Finally, the intramolecular mechanism (TS5) has the highest

https://doi.org/10.1021/acscatal.2c03844
ACS Catal. 2022, 12, 14227−14242

activation energy (134 kJ·mol^{-1}) and the deprotonation of the *ortho*-protonated phenol formed in the reaction was then no longer investigated. Overall, the main mechanistic features of the reaction are preserved with respect to the alkylation of benzene with ethene, for which Wang et al.[29] obtained a qualitatively similar profile using static simulations at a PBE-D3 level of theory.

Similar considerations can be made for the reaction profile of 4-*n*-PP (Figure 5b). Interestingly, the reaction barriers related to the C−C bond scission (TS2, TS4, and TS5) are all lower than in the 4-EP case (−5 kJ·mol^{-1} for TS2, −25 kJ·mol^{-1} for TS4 and TS5). As expected, forming a more substituted alkene (isopropene *vs* ethene) is energetically advantageous. Despite its comparably lower stabilization, TS2 remains the most favorable dealkylation path, with an activation energy of 96 kJ·mol^{-1}. 102 kJ·mol^{-1} is needed to reach TS4 from the most stable Wheland complex state, while the intramolecular TS5 has again the highest activation free energy, *i.e.*, 109 kJ·mol^{-1}. The transition-state geometries are quite similar to 4-EP, where we however observed a small but systematic increase in the C−C or C−O bond that must be broken to form isopropene (0.06−0.07 Å, Figure 6)

When comparing the profiles for 4-EP and 4-*n*-PP, our results show that when starting from the neutral adsorbed reactants, 133 kJ·mol^{-1} is needed to reach TS2 for 4-EP and 132 kJ·mol^{-1} for 4-*n*-PP (141 and 135 kJ·mol^{-1} starting from the gas-phase reactants, Table 1). This difference is very small and largely within the typical DFT uncertainty. However, when comparing the reaction barriers, there is a clear decrease in the barriers when moving from 4-EP to 4-*n*-PP, which is in line with the moderate reduction in temperature required experimentally to reach 50% conversion (from ∼650 K for 4-EP to ∼575 K for 4-*n*-PP). On the other hand, experimental kinetic analysis of the reaction showed that 4-EP has an apparent activation energy of 60±3 kJ·mol^{-1}, while 4-*n*-PP has an apparent activation energy of 98 ± 6 kJ·mol^{-1}, with the observed increase in rate mainly due to entropic reasons.[15] This large difference was tentatively attributed to the different heat of adsorption between the two molecules, as when considering their dehydroxylated counterparts, ethylbenzene has a higher heat of adsorption than *n*-propylbenzene.[76,77] This large difference in adsorption energy does not clearly emerge from our computations, where 4-*n*-PP has an adsorption enthalpy of −135 kJ·mol^{-1}, while 4-EP has an adsorption enthalpy of −121 kJ·mol^{-1} (Table S1), a difference mainly originating from the difference in dispersive interactions. It seems then that other factors must be into play when comparing the theory results with the experimental kinetic data. The likelier source of error could lie in our estimate of the adsorption enthalpy, which might be heavily biased when working in the harmonic approximation and accounting for a single conformation of a relatively mobile adsorbate.[78] In principle, one could go beyond this approach using MD simulations and a higher level of theory to more accurately account for long-range interactions.[79,80] This is however well beyond the scope of the present study.

Finally, 4-*iso*-PP presents, in general, very reduced barriers (green scheme in Figure 5) with respect to the other two reactants. Only 66 kJ·mol^{-1} is needed to activate TS2 and TS3, while TS4 proceeds with an activation energy of 61 kJ·mol^{-1}. As in the previous cases, the formation of the surface alkoxide is endergonic, leading to an overall barrier of 85 kJ·mol^{-1} to undergo stepwise dealkylation. The intramolecular dealkylation still has a very high activation energy compared to the other mechanisms (105 kJ·mol^{-1}). Therefore, also in this case, the concerted path is computed to be the lowest activated. Furthermore, the large decrease in activation energy (only 100 kJ·mol^{-1} separate the gas-phase reactants from TS2, see Table 1) agrees very well with the experiment, where almost full conversion was reached already at less than 500 K. The transition-state geometries of TS2, TS4, and TS5 present very elongated bond lengths (∼3 Å, Figure 6) indicating—not surprisingly—a larger charge accumulation on the more substituted reactive carbon. The increase in stability moving from primary to secondary carbenium ions is sufficient to create, for both TS2 and TS4, a metastable isopropyl cation moiety that was formed in the optimization toward the reactant basin (Figure 5). Frequency analysis revealed that this is indeed a minimum. However, a minimal perturbation of the C−C (for TS2) or C−O (for TS4) bond length followed by a geometry optimization brings the system in the expected reactant state, confirming that the isopropyl cation minimum is extremely shallow.

Our calculations show overall a good qualitative agreement with the reactivity differences observed experimentally. For 4-*iso*-PP, the pronounced reactivity is easily explained by the stabilization of the transition states caused by the double hyperconjugation with the methyl groups. The stabilization is strong enough to make the isopropyl cation a possible metastable intermediate for the reaction. In the 4-*n*-PP case, the methyl group cannot directly conjugate with the carbon on which the partial positive charge is located. Nevertheless, it can still interact with the forming π orbital of the incipient double bond, stabilizing both the transition state and the produced substituted olefin. While this is possibly not the main reason for the increase in reactivity observed experimentally, it indicates that 4-*n*-PP should be intrinsically slightly more reactive that 4-EP toward dealkylation. A similar trend was also observed by Arstad et al.[26] for the alkylation of benzene with ethene and propene over a cluster model of the zeolite.

From a mechanistic perspective, it is very likely for all of the investigated reactants to undergo concerted dealkylation (TS2), as the energy requirement is in all cases lower than TS4. Differently from the ethylation of benzene, the concerted path does not require the substrate and ethylating agent to come together in proximity of the active site, which was found to potentially hamper the reaction progress and favor the stepwise path.[29] On the other hand, SAS formation (in equilibrium with the Wheland complex and neutral alkylphenol) seems plausible, TS3 being similar in energy with respect to TS2, but the endergonic character of the reaction makes its concentration in the pores likely small. This is potentially different than in benzene ethylation, where the stepwise path becomes more favorable at high ethylating agent concentrations and where the presence of surface ethoxide species was detected through NMR spectroscopy.[32]

While demethoxylation of the lignin compounds can lead to the alkylphenols investigated so far (Figure 1), it has also recently been shown that the alkylcatechol compounds obtained after O-demethylation of the lignin-derived alkylguaiacols can also be C-dealkylated in a similar fashion.[17] To understand the effect of a second hydroxyl substituent on the aromatic ring, we also recomputed the dealkylation mechanism of 4-EC. All transition states were reoptimized except for TS4, as it does not directly involve the aromatic moiety and thus we did not expect any significant change in its energy. The free-

https://doi.org/10.1021/acscatal.2c03844
ACS Catal. 2022, 12, 14227−14242

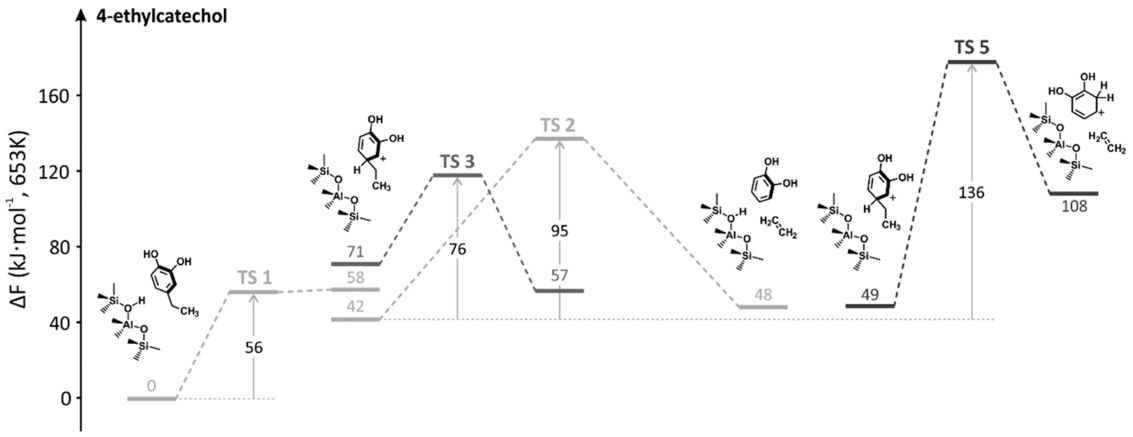

Figure 7. Free-energy profiles (653 K) for all possible dealkylation mechanisms of 4-EC. The reference value for the free energies corresponds to the empty zeolites and the reacting 4-EC in gas phase. Activation energies and free energies of the intermediates are reported in kJ·mol^{-1}. For the sake of clarity, TS5 is reported on the right of the profiles, despite its reactant state corresponding to the reactant states of TS2 and TS3.

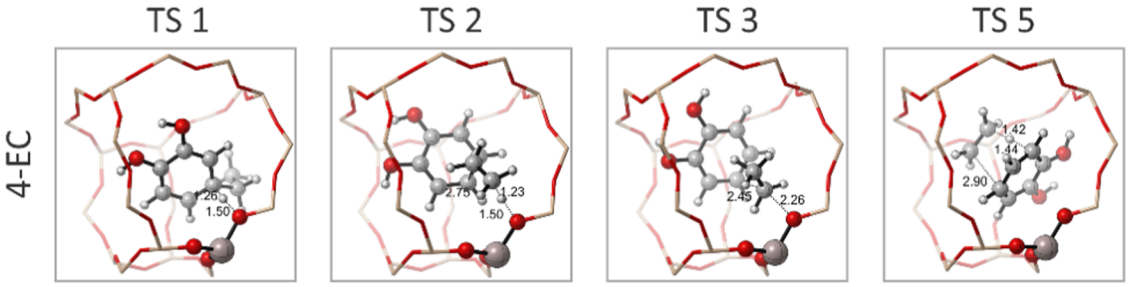

Figure 8. Relaxed transition-state geometries for the dealkylation of 4-EC. Relevant distances are reported in Å. The shown framework portion is the same as in Figure 6.

energy profile is shown in Figure 7, while the geometry of the transition states is shown in Figure 8.

The protonation step (TS1) has a moderately higher activation energy with respect to 4-EP (56 *vs* 46 kJ·mol^{-1}). The free energies of the products of TS1 are slightly higher in energy than the transition state (Figure 7), which is an artifact caused by the approximations in the frequency calculations on one particular configuration of the products resulting from TS1. Indeed, when comparing the 0 K electronic energy of the protonated arenium ion, the product is indeed lower in energy than the transition state.

TS3 is surprisingly low in energy, with a barrier of only 76 kJ·mol^{-1}. The C−C distance is somehow more stretched than in the 4-EP case (2.45 *vs* 2.40 Å, compare Figures 6 and 8), while the C−O distance remains almost unaffected. However, the product SAS remains higher in energy (+15 kJ·mol^{-1}) compared to the most stable Wheland intermediate. This value, combined with the 4-EP activation energy of TS4, leads to an overall barrier of 120 kJ·mol^{-1} to overcome in the stepwise path. Therefore, also here, the concerted pathway would be preferred.

When comparing the overall activation energies for 4-EC and 4-EP, the differences are relatively small (137 *vs* 132 kJ·mol^{-1} with respect to the neutral reactants are found for 4-EC and 4-EP, respectively) and certainly well beyond the methodological accuracy. Therefore, we can conclude that the effect of a second hydroxyl group on the aromatic ring—if any—is very small. This is in line with the experimental observations, where the dealkylation of 4-*n*-propylcatechol occurs at analogous temperature as the dealkylation of 4-*n*-PP.

Before moving on with the final section, some interesting observations about the connection between our calculations and the realistic reaction environment can be made, in particular, concerning the water coverage. Because of their strong interaction with the BAS, adsorbed water molecules can interfere with the kinetics of proton transfer reactions, both by acting as proton shuttling medium as well as by fully solvating the BAS as hydronium ion (compare with the following section). Recently, we indeed showed that low water coverages (1−3 molecules per BAS) can significantly speed up the protonation reaction of aromatic hydrocarbons in H-ZSM-5, helping the proton shuttling from the framework to the molecule.[20] At higher coverages (6 molecules per BAS), the rate goes back to similar values as in the anhydrous case. Since there are no reasons to suspect very different behaviors for the four considered reactants, it seems plausible that the kinetics of TS1 will be affected in a similar fashion by the presence of coadsorbed water. Therefore, even if the absolute values of the free-energy barriers could change, it seems unlikely that this will affect the computed reactivity trends.

The possible water effect is less clear on the actual dealkylation transition states. For this reason, TS2 (for 4-EP, 4-*n*-PP, and 4-*iso*-PP) was further investigated by means of dynamic US simulations in the presence of three water molecules coadsorbed in the zeolite unit cell. For a complete discussion of the results, the interested reader is referred to Section S4. While the reactivity trends across the reactants do not seem to be particularly affected, it was found that the dealkylation reaction competes with the deprotonation of the Wheland complex hydroxyl group to form a 4-alkyl-2,5-cyclohexadienone moiety. The deprotonation occurs preferen-

https://doi.org/10.1021/acscatal.2c03844
ACS Catal. 2022, 12, 14227−14242

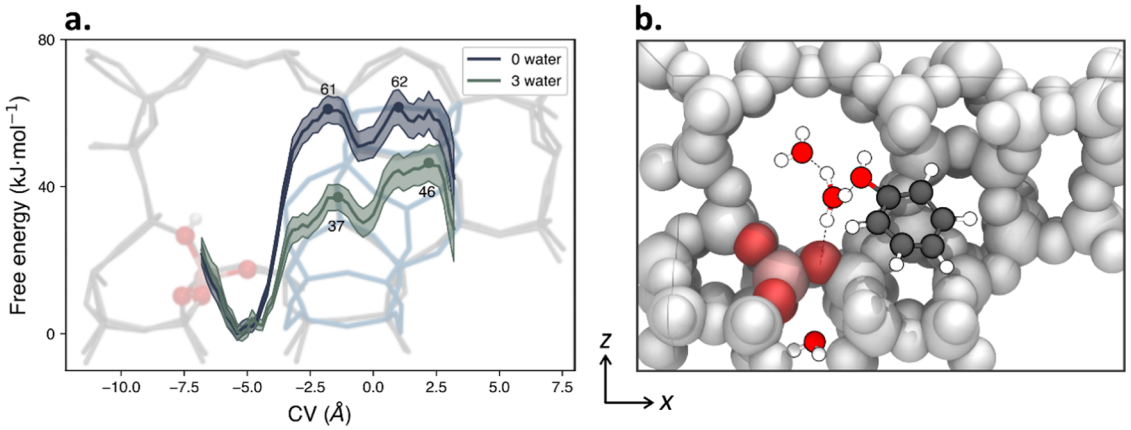

Figure 9. (a) Free-energy profile for the diffusion of phenol along the straight channel of H-ZSM-5 with zero and three water molecules in the zeolite unit cell. The image in the background shows the rough location of the various CV values within the framework, where the Al tetrahedra and BAS location are highlighted in ball-and-stick representation, while the double ring separating the two channel intersections in light blue. (b) Snapshot arbitrarily extracted from the umbrella centered at CV = −1.5, where the H-ZSM-5 unit cell is seen along the straight channel. It is possible to see how the water maintains an interaction with the phenol hydroxyl group, thereby assisting the diffusion.

tially when multiple water molecules interact with the hydroxyl group, in line with the higher proton affinity of water clusters with high molecularity.[20,35,36] The deprotonated form is not particularly stable ($\Delta F \sim +70$ kJ·mol^{-1}) and it is indeed not observed in the 4-*iso*-PP case where the dealkylation barrier is lower in magnitude. On the other hand, it is possible that at higher water loadings, the O-deprotonation of the reactants could become more favorable. Since the neutral form cannot undergo dealkylation, an equilibrium between the Wheland complex and 4-alkyl-2,5-cyclohexadienone could be tentatively indicated as a cause for the increase in Arrhenius activation energy for the 4-*n*-PP dealkylation observed experimentally in the presence of water.[15]

3.3. Effect of Water on Phenol Diffusion. Differently from traditional hydrocarbon chemistry, alkylphenols dealkylation requires to cofeed steam in the reactants stream to prevent a quick and reversible deactivation of the catalyst. This was attributed to water preventing the condensation of phenol to diphenylether, but it was also speculated that it could facilitate desorption of phenol from the catalyst. The reaction barriers computed for the diphenylether formation mechanism in anhydrous conditions are of similar magnitude as the dealkylation ones, in line with a fast build-up of the molecule in the catalyst pores (for a complete overview of the results, see Section S6). Since water is formed as the reaction product, the presence of steam will help to shift the reaction equilibrium toward the reacting phenols. On the other hand, it is less clear as to how far water could enhance the diffusion and desorption of the latter from the zeolite framework. Therefore, the role of water in modulating phenol diffusion along the straight channels of H-ZSM-5 was investigated by means of four separate umbrella sampling simulations, with water loadings varying from 0 to 3 water molecules per unit cell. Larger water clusters (up to 8 molecules/BAS) have been observed in the zeolite at high water partial pressures and low temperatures[81] and water is also known to adsorb quite nonhomogeneously on the BAS.[82] Nonetheless, the free-energy profiles with two and three water molecules are fundamentally indistinguishable, making it unlikely that a higher coverage would significantly affect the results (*vide infra*). Since the results related to the simulations with one and two water molecules were found to be intermediate between the zero and three water cases, only the latter will be discussed in detail. For a complete overview of the results across all loadings, the interested reader is referred to Section S5.4. Diffusion through the sinusoidal channel was not considered as it is known to be significantly slower, based on both theoretical and experimental evidence.[37,83] For instance, based on a set of static simulations, DeLuca and Hibbits found that the diffusion barrier for toluene in all-silica MFI increases from 15 to 56 kJ·mol^{-1} when moving from the straight to the sinusoidal channel.[37]

The obtained free-energy profiles for phenol diffusion along the H-ZSM-5 straight channel with zero and three water molecules are shown in Figure 9a.

The main feature that emerges from the simulated FEPs is the significant reduction in the diffusion barrier computed in the presence of water. The barrier to diffuse through the straight channel in the anhydrous case amounts to 61 kJ·mol^{-1}, whereas in the presence of three water molecules in the zeolite unit cell, the barrier is reduced to only 37 kJ·mol^{-1}. Importantly, phenol also has to desorb from the BAS to travel through the straight channel, an effect contributing to the overall free-energy profile. When traveling through the straight channel, the molecule encounters two skewed 10-membered rings, which separate the channel intersections. The maxima in the profile originate from the actual crossing of the two 10-membered rings. In both the anhydrous and hydrated cases, the FEP has a shallow minimum located in between the two skewed 10-membered rings. A similar behavior has been recently reported for aromatic diffusion in all-silica MFI by DeLuca and Hibbitts,[37] where two minima around the channel center were observed instead for benzene diffusion. The presence of a single minimum in our FEP is likely due to the dynamic nature of the simulation and the asymmetric nature of phenol. Indeed, the phenol oxygen also being included in the computation of the molecule center (Figure 3), its orientation can produce different CV values that are associated with a similar position of the aromatic ring in the channel. This effect can produce a "blurring" when moving from well-defined states on the PES to an averaged FEP.

When comparing the two FEPs, it is observed that the profile is quite symmetric in the anhydrous case and that the second transition state to travel through the second 10-membered ring is nearly isoenergetic with the first (61 *vs* 62 kJ·

https://doi.org/10.1021/acscatal.2c03844
ACS Catal. 2022, 12, 14227−14242

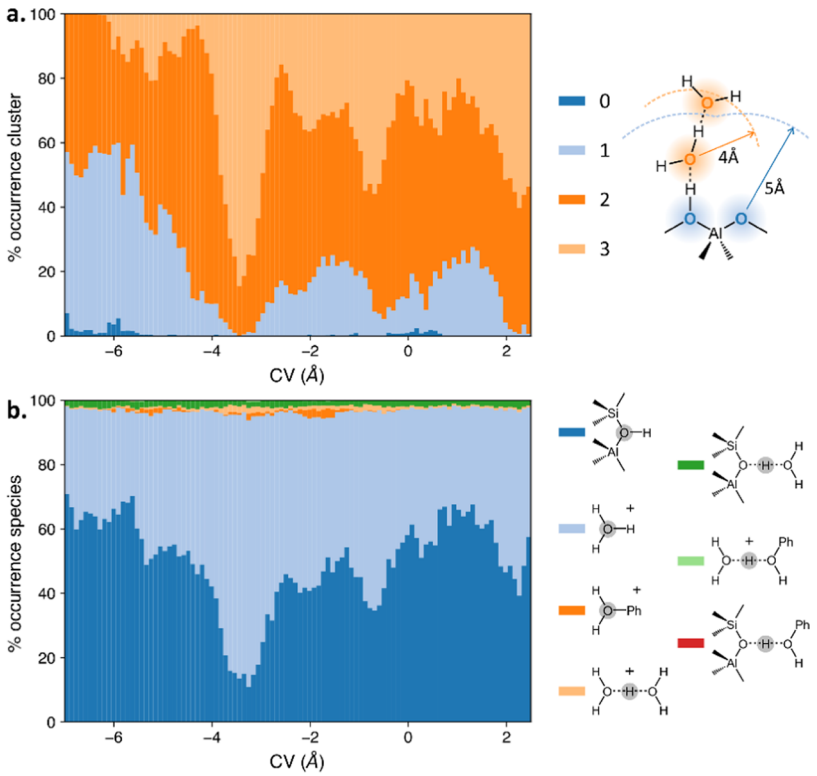

Figure 10. (a) Percentage of occurrence of a certain water cluster size in proximity of the active site as a function of the US CV. The scheme on the right sketches how the cluster size is computed, by first searching for water molecules within a 5 Å cutoff from the zeolite oxygen atoms in the first coordination sphere of the Al site and then, starting from the closer water, looking for other water molecules within 4 Å and so on until no further water molecules can be found. (b) Percentage of occurrence of the various possible protonated species during the US simulations as a function of the US CV. The atom highlighted in gray in the legend shows the location of the fictitious proton atom in various cases (see main text). In both cases, the trajectory is subsampled every 2.5 fs.

mol^{-1}). This seems to indicate that, once the phenol reaches the first barrier, its interaction with the BAS has already completely vanished and diffusing even further from it does not require additional energy. On the other hand, when water is present in the unit cell, the FEP becomes significantly asymmetric and the barrier to cross the second ring increases to 46 $kJ \cdot mol^{-1}$. When looking at the simulations, it was noticed that water tends to form a chain of hydrogen bonds between the active site and the diffusing phenol molecule (Figure 9b). Only when moving even further along the straight channel (CV > 0), this chain of H-bonds begins to get stretched, causing the moderate energy increase to cross the second ring. We remark that previous considerations are mostly qualitative as the actual energy barriers might vary due to error bars of the simulations. Despite not being directly comparable, the activation free energies for phenol diffusion computed in the presence of water are largely lower than the static (but also dynamic, see Section S4) barrier of the dealkylation process for 4-EP and 4-*n*-PP, in line with the experimental observation that the reaction kinetics does not seem to be diffusion-limited for 4-*n*-PP.[15] This might not be the case for 4-*iso*-PP, as the hindrance of the isopropyl tail reduces its mobility in the framework (Figure S3) while, at the same time, leading to reduced dealkylation barriers.

To better understand the reasons underlying the large difference in diffusion barriers with different water loadings, we assessed whether the water molecules (whose position is not restrained during the simulations) do remain in proximity of the BAS and the diffusing phenol. A cutoff radius of 5 Å was defined around the O atoms in the first coordination sphere of the Al defect. If no water molecules are found within such a radius, the cluster size is set to 0. Otherwise, the closest water molecule is taken as reference and a second cutoff radius of 4 Å is defined around it. All water molecules included in such a cutoff are then added to the cluster size and are then used as new centers to look for other water molecules until no others are found. This procedure was done for every umbrella trajectory (subsampling it every 2.5 fs to make the amount of data more manageable) and the percentage of occurrence of each cluster size reported as a function of the US CV (Figure 10a). A cluster size of 0 is almost never observed during the simulations, indicating that water strongly interacts with the BAS—as expected. In the simulations with one water molecule, it is more likely for the water to diffuse away from the active site. On the other hand, even for low CV values, the phenol molecule is not capable of completely displacing the water molecule, which is far from the Al substitution at most 60−70% of the times for CV < −6 Å (Figure S13a). This percentage is largely reduced moving to two waters and basically disappears with three waters, where at least one water molecule remains in the BAS proximity for more than 90% of the simulation time at any considered CV value. When phenol moves away from the active site (increasing CV values), water does not have any competition to access the BAS and cluster sizes of larger molecularity become predominant. Quite some fluctuation is observed in the cluster sizes while moving toward higher CV values. We attribute this to the fact that the data comes from separate umbrellas, and in some of them, larger

https://doi.org/10.1021/acscatal.2c03844
ACS Catal. 2022, 12, 14227−14242

cluster sizes are preserved most of the simulation time, while for the others, more diffusive events are observed. This is very likely a random process and, water diffusion being relatively slow with respect to our simulation times, it is not possible to achieve a fully equilibrated distribution of cluster sizes in all umbrellas. The observation of various cluster sizes also indicates that considering more molecules per unit cell is not necessary as, if much larger cluster sizes would be favorable, we would almost never observe the three molecules diffusing away from the active site.

Having assessed that water remains in proximity of the active site during the simulations, we investigated how the BAS interacts with the protic molecules present in the unit cell. We first defined the location of a fictitious proton atom using a combination of the collective variables proposed by Pérez de Alba Ortíz et al.[84] and Grifoni et al.[85] (for more information, see Section S5.3). In this approach, such a fictitious atom is located on the oxygen carrying an excess of hydrogen atoms with respect to a selected default value (for instance, 2 for a water oxygen or 0 for a zeolite oxygen). To practically visualize how the location of the proton atom evolves during a simulation, we invite the interested reader to refer to the movie in the Supporting Information, which shows the 40−50 ps interval of the umbrella centered at $CV_0 = 0.0$ with three water molecules. We then computed, in each simulation, where this proton atom is located with respect to the proton-acceptor species and used this data to obtain the percentage of occurrence of a determined protonated species (Figure 10b).

What immediately emerges from the figure is that two states dominate the simulation in all of the umbrellas, with the extra proton being either located on the zeolite (thus a "regular" BAS) or on a water molecule, forming an eigen-like hydronium ion (H_3O^+). The balance between the two is dictated by the amount of water molecules in proximity of the active site (compare the similar up-down trends in the top and bottom graphs of Figure 10 and with the results obtained at different water loadings in Figure S13b) as it is well-known that at least two water molecules are required to lead to a significant solvation of the BAS.[35,36] Phenol seems, on the other hand, to have a much more limited interaction with the BAS. As it can be seen, the instances in which its hydroxyl group is protonated are very infrequent (<10%) even when in close proximity of the Al site.

Interestingly, it can be seen how the calculations predict that the proton is preferentially located on a specific atom and the sampling of structures in which it is shared between two atoms (Zundel-like ions) is very small independently on the phenol location. According to these results, phenol and water are then in direct competition for the zeolite active site and this will certainly favor the desorption and diffusion of the former. Further insights in this behavior were obtained by computing the adsorption enthalpies for coadsorption of phenol and one water molecule with static simulations (an extensive discussion of the results is reported in Section S5.5). The computed adsorption enthalpy for phenol decreases from 132 to 113 kJ·mol^{-1} if water is coadsorbed on the BAS while, at the same time, the adsorption enthalpy of water also decreases from 83 to 64 kJ·mol^{-1} if phenol is coadsorbed on the BAS. This suggests that competitive coadsorption penalizes both molecules with respect to a single-molecule adsorption and thus not only does water enhance the kinetics of phenol diffusion but it also modulates its adsorption thermodynamics.

In Figure 10b, it can be seen that protonated phenol seldomly occurs up to relatively high CV values, where a direct transfer of the BAS from the framework would no longer be possible. This is caused by water that, as the phenol diffuses away from the active site, creates a chain of hydrogen bonds along which the extra proton is allowed to move (Figure 9b). Furthermore, spontaneous *ortho* protonation of phenol was observed in the anhydrous case when located close to the BAS (in umbrellas 1 and 2, see Table S1) after about 10 ps of simulation and the so-formed arenium ion proved to be stable for the rest of the simulation. Phenol protonation was also observed with one and two water molecules in the unit cell, but not with three (Figure S13b), indicating that larger loadings could also have an active effect on the formation of protonated phenolic species, as already highlighted in the case of ethylbenzene protonation.[20]

Calculations then suggest that not only does water compete with phenol to directly adsorb on the BAS, thereby facilitating its desorption, but it also assists its diffusion through the straight zeolite channel by forming a chain of H-bonds thanks to which the phenol hydroxyl group does not have to completely break its interaction with the active site when crossing between the two channel intersections.

4. CONCLUSIONS

In this work, we have explored the two main features of the H-ZSM-5-catalyzed alkylphenol dealkylation reaction. Through a combination of static and dynamic DFT simulations, we showed that 4-*iso*-PP is much more reactive than 4-*n*-PP and 4-EP, as the secondary nature of the central carbon atom of the isopropyl tail stabilizes the (partially) positively charged transition states. 4-*n*-PP presents somehow lower activation energies than 4-EP, in line with the experimentally observed reactivity trends, although the latter also suggests the decrease in reactivity to be mainly entropic in nature. This could be due to contributions deriving from the adsorption step of the reactant in the zeolite, which is however outside the scope of this contribution. Mechanistically, we found that the reaction proceeds mainly through a concerted mechanism, being characterized by the lowest computed activation energy; however, the formation of surface alkoxide species is also possible in low amounts. Umbrella sampling simulations of the dealkylation reaction in the presence of three water molecules showed that the intermediate Wheland complex can be O-deprotonated by the water cluster. This reaction competes with dealkylation for 4-EP and 4-*n*-PP, being possibly one of the reasons underlying the higher activation energies measured experimentally in the presence of steam.

Umbrella sampling was also used to investigate the mobility of the phenol product along the straight zeolite channel in anhydrous conditions and with one, two, and three water molecules in the unit cell. We found that water may play an important role in assisting phenol desorption and diffusion away from the zeolite BAS, with a computed decrease in the free-energy barrier from 62 to 46 kJ·mol^{-1} when moving from zero to three coadsorbed molecules. This is caused by the competitive adsorption of water and phenol on the BAS. Water is shown to preferentially interact with the BAS, thereby effectively shielding it from phenol. On the other hand, it also appears that a chain of water-mediated hydrogen bonds between the BAS and the phenol can be formed while the latter is diffusing, which could assist its passage between the two channel intersections. The assistance of water in

https://doi.org/10.1021/acscatal.2c03844
ACS Catal. 2022, 12, 14227−14242

desorption and diffusion away from the BAS could lead to shorter residence times of phenolic compounds in the zeolite, preventing their condensation to bulkier biphenylether species. It would be interesting to explore in future studies as to how far this behavior is extendable to other (moderately) bulky and polar molecules diffusing along the straight channels of the H-ZSM-5 zeolite and to provide further atomistic details in the role played by water in modulating the kinetics of relevant zeolite-catalyzed reactions.

■ ASSOCIATED CONTENT

Supporting Information

The Supporting Information is available free of charge at https://pubs.acs.org/doi/10.1021/acscatal.2c03844.

Catalyst model, extended details on the behavior and stability of reaction intermediates from the unbiased MD simulations, explicit values of the free energy (with enthalpic and entropic contributions) for all of the optimized stationary points, and extended details on the US simulations of TS2 in the presence of three water molecules on the diffusion of phenol with one and two water molecules and on the mechanism of phenol condensation to diphenylether (PDF)

Movie showing the location of the fictitious proton atom (orange sphere) in the 40−50 ps interval taken from the simulation of the umbrella centered at CV_0 = 0.0 Å (MP4)

POSCAR of all of the optimized stationary points reported in the manuscript; Cartesian coordinates of the initial structures for the US simulations; CP2K and PLUMED input file examples (ZIP)

■ AUTHOR INFORMATION

Corresponding Author

Veronique Van Speybroeck − *Center for Molecular Modeling, Ghent University, 9052 Zwijnaarde, Belgium;* orcid.org/0000-0003-2206-178X;
Email: Veronique.Vanspeybroeck@Ugent.be

Author

Massimo Bocus − *Center for Molecular Modeling, Ghent University, 9052 Zwijnaarde, Belgium;* orcid.org/0000-0001-9474-6644

Complete contact information is available at: https://pubs.acs.org/10.1021/acscatal.2c03844

Notes

The authors declare no competing financial interest.

■ ACKNOWLEDGMENTS

The authors acknowledge the Fund for Scientific Research—Flanders (FWO, BioFact Excellence of Science project G0H0918N, ID EOS: 30902231, and project G024019N) as well as the Research Board of Ghent University (BOF). The computational resources (Stevin Supercomputer Infrastructure) and services used in this work were provided by the VSC (Flemish Supercomputer Center), funded by the Ghent University, FWO, and the Flemish Government—Department of EWI.

■ REFERENCES

(1) Chu, S.; Majumdar, A. Opportunities and Challenges for a Sustainable Energy Future. *Nature* **2012**, *488*, 294−303.
(2) Martens, J. A.; Bogaerts, A.; De Kimpe, N.; Jacobs, P. A.; Marin, G. B.; Rabaey, K.; Saeys, M.; Verhelst, S. The Chemical Route to a Carbon Dioxide Neutral World. *ChemSusChem* **2017**, *10*, 1039−1055.
(3) Weissermel, K.; Arpe, H.-J.*Industrial Organic Chemistry*, 4th ed.; Wiley-VCH Verlag GmbH: Weinheim, Germany, 2003.
(4) Zakzeski, J.; Bruijnincx, P. C. A.; Jongerius, A. L.; Weckhuysen, B. M. The Catalytic Valorization of Lignin for the Production of Renewable Chemicals. *Chem. Rev.* **2010**, *110*, 3552−3599.
(5) Calvo-Flores, F. G.; Dobado, J. A. Lignin as Renewable Raw Material. *ChemSusChem* **2010**, *3*, 1227−1235.
(6) Li, C.; Zhao, X.; Wang, A.; Huber, G. W.; Zhang, T. Catalytic Transformation of Lignin for the Production of Chemicals and Fuels. *Chem. Rev.* **2015**, *115*, 11559−11624.
(7) Renders, T.; Van den Bossche, G.; Vangeel, T.; Van Aelst, K.; Sels, B. Reductive Catalytic Fractionation: State of the Art of the Lignin-First Biorefinery. *Curr. Opin. Biotechnol.* **2019**, *56*, 193−201.
(8) Liao, Y.; Koelewijn, S. F.; van den Bossche, G.; van Aelst, J.; van den Bosch, S.; Renders, T.; Navare, K.; Nicolaï, T.; van Aelst, K.; Maesen, M.; et al. A Sustainable Wood Biorefinery for Low-Carbon Footprint Chemicals Production. *Science* **2020**, *367*, 1385−1390.
(9) Van Den Bosch, S.; Schutyser, W.; Koelewijn, S. F.; Renders, T.; Courtin, C. M.; Sels, B. F. Tuning the Lignin Oil OH-Content with Ru and Pd Catalysts during Lignin Hydrogenolysis on Birch Wood. *Chem. Commun.* **2015**, *51*, 13158−13161.
(10) Van Den Bosch, S.; Schutyser, W.; Vanholme, R.; Driessen, T.; Koelewijn, S. F.; Renders, T.; De Meester, B.; Huijgen, W. J. J.; Dehaen, W.; Courtin, C. M.; et al. Reductive Lignocellulose Fractionation into Soluble Lignin-Derived Phenolic Monomers and Dimers and Processable Carbohydrate Pulps. *Energy Environ. Sci.* **2015**, *8*, 1748−1763.
(11) Schutyser, W.; Renders, T.; Van Den Bosch, S.; Koelewijn, S. F.; Beckham, G. T.; Sels, B. F. Chemicals from Lignin: An Interplay of Lignocellulose Fractionation, Depolymerisation, and Upgrading. *Chem. Soc. Rev.* **2018**, *47*, 852−908.
(12) Sun, Z.; Fridrich, B.; De Santi, A.; Elangovan, S.; Barta, K. Bright Side of Lignin Depolymerization: Toward New Platform Chemicals. *Chem. Rev.* **2018**, *118*, 614−678.
(13) Verboekend, D.; Liao, Y.; Schutyser, W.; Sels, B. F. Alkylphenols to Phenol and Olefins by Zeolite Catalysis: A Pathway to Valorize Raw and Fossilized Lignocellulose. *Green Chem.* **2016**, *18*, 297−306.
(14) Liao, Y.; D'Halluin, M.; Makshina, E.; Verboekend, D.; Sels, B. F. Shape Selectivity Vapor-Phase Conversion of Lignin-Derived 4-Ethylphenol to Phenol and Ethylene over Acidic Aluminosilicates: Impact of Acid Properties and Pore Constraint. *Appl. Catal., B* **2018**, *234*, 117−129.
(15) Liao, Y.; Zhong, R.; Makshina, E.; d'Halluin, M.; van Limbergen, Y.; Verboekend, D.; Sels, B. F. Propylphenol to Phenol and Propylene over Acidic Zeolites: Role of Shape Selectivity and Presence of Steam. *ACS Catal.* **2018**, *8*, 7861−7878.
(16) Liao, Y.; Zhong, R.; D'Halluin, M.; Verboekend, D.; Sels, B. F. Aromatics Production from Lignocellulosic Biomass: Shape Selective Dealkylation of Lignin-Derived Phenolics over Hierarchical ZSM-5. *ACS Sustainable Chem. Eng.* **2020**, *8*, 8713−8722.
(17) Wu, X.; Liao, Y.; Bomon, J.; Tian, G.; Bai, S.-T.; Van Aelst, K.; Zhang, Q.; Vermandel, W.; Wambacq, B.; Maes, B. U. W.; et al. Lignin-First Monomers to Catechol: Rational Cleavage of C-O and C-C Bonds over Zeolites. *ChemSusChem* **2021**, No. e202102248.
(18) Van Der Mynsbrugge, J.; Moors, S. L. C.; De Wispelaere, K.; Van Speybroeck, V. Insight into the Formation and Reactivity of Framework-Bound Methoxide Species in h-Zsm-5 from Static and Dynamic Molecular Simulations. *ChemCatChem* **2014**, *6*, 1906−1918.
(19) Nastase, S. A. F.; Cnudde, P.; Vanduyfhuys, L.; De Wispelaere, K.; Van Speybroeck, V.; Catlow, C. R. A.; Logsdail, A. J. Mechanistic Insight into the Framework Methylation of H-ZSM-5 for Varying

Methanol Loadings and Si/Al Ratios Using First-Principles Molecular Dynamics Simulations. *ACS Catal.* **2020**, *10*, 8904−8915.
(20) Bocus, M.; Vanduyfhuys, L.; De Proft, F.; Weckhuysen, B. M.; Van Speybroeck, V. Mechanistic Characterization of Zeolite-Catalyzed Aromatic Electrophilic Substitution at Realistic Operating Conditions. *JACS Au* **2022**, *2*, 502−514.
(21) Van Speybroeck, V.; De Wispelaere, K.; Van Der Mynsbrugge, J.; Vandichel, M.; Hemelsoet, K.; Waroquier, M. First Principle Chemical Kinetics in Zeolites: The Methanol-to-Olefin Process as a Case Study. *Chem. Soc. Rev.* **2014**, *43*, 7326−7357.
(22) Van Speybroeck, V.; Hemelsoet, K.; Joos, L.; Waroquier, M.; Bell, R. G.; Catlow, C. R. A. Advances in Theory and Their Application within the Field of Zeolite Chemistry. *Chem. Soc. Rev.* **2015**, *44*, 7044−7111.
(23) Jansang, B.; Nanok, T.; Limtrakul, J. Structure and Reaction Mechanism of Alkylation of Phenol with Methanol over H-FAU Zeolite: An ONIOM Study. *J. Phys. Chem. C* **2008**, *112*, 540−547.
(24) Nie, X.; Janik, M. J.; Guo, X.; Liu, X.; Song, C. Reaction Mechanism of Tert-Butylation of Phenol with Tert-Butyl Alcohol over H-β Zeolite: An ONIOM Study. *Catal. Today* **2011**, *165*, 120−128.
(25) Vos, A. M.; Schoonheydt, R. A.; De Proft, F.; Geerlings, P. Reactivity Descriptors and Rate Constants for Acid Zeolite Catalyzed Ethylation and Isopropylation of Benzene. *J. Phys. Chem. B* **2003**, *107*, 2001−2008.
(26) Arstad, B.; Kolboe, S.; Swang, O. Theoretical Investigation of Arene Alkylation by Ethene and Propene over Acidic Zeolites. *J. Phys. Chem. B* **2004**, *108*, 2300−2308.
(27) Hansen, N.; Brüggemann, T.; Keil, F. J.; Bell, A. T. Theoretical Investigation of Benzene Alkylation with Ethene over H-ZSM-5. *J. Phys. Chem. C* **2008**, *112*, 15402−15411.
(28) Hansen, N.; Kerber, T.; Sauer, J.; Bell, A. T.; Keil, F. J. Quantum Chemical Modeling of Benzene Ethylation over H-ZSM-5 Approaching Chemical Accuracy: A Hybrid MP2:DFT Study. *J. Am. Chem. Soc.* **2010**, *132*, 11525−11538.
(29) Wang, D.; Wang, C. M.; Yang, G.; Du, Y. J.; Yang, W. M. First-Principles Kinetic Study on Benzene Alkylation with Ethanol vs. Ethylene in H-ZSM-5. *J. Catal.* **2019**, *374*, 1−11.
(30) Chen, W.; Yi, X.; Liu, Z.; Tang, X.; Zheng, A. Carbocation Chemistry Confined in Zeolites: Spectroscopic and Theoretical Characterizations. *Chem. Soc. Rev.* **2022**, *51*, 4337−4385.
(31) Gong, X.; Çağlayan, M.; Ye, Y.; Liu, K.; Gascon, J.; Dutta Chowdhury, A. First-Generation Organic Reaction Intermediates in Zeolite Chemistry and Catalysis. *Chem. Rev.* **2022**, *122*, 14275−14345.
(32) Chowdhury, A. D.; Houben, K.; Whiting, G. T.; Chung, S. H.; Baldus, M.; Weckhuysen, B. M. Electrophilic Aromatic Substitution over Zeolites Generates Wheland-Type Reaction Intermediates. *Nat. Catal.* **2018**, *1*, 23−31.
(33) Kolboe, S.; Svelle, S.; Arstad, B. Theoretical Study of Ethylbenzenium Ions: The Mechanism for Splitting off Ethene, and the Formation of a π Complex of Ethene and the Benzenium Ion. *J. Phys. Chem. A* **2009**, *113*, 917−923.
(34) Collinge, G.; Yuk, S. F.; Nguyen, M. T.; Lee, M. S.; Glezakou, V. A.; Rousseau, R. Effect of Collective Dynamics and Anharmonicity on Entropy in Heterogenous Catalysis: Building the Case for Advanced Molecular Simulations. *ACS Catal.* **2020**, *10*, 9236−9260.
(35) Liu, P.; Mei, D. Identifying Free Energy Landscapes of Proton-Transfer Processes between Brønsted Acid Sites and Water Clusters Inside the Zeolite Pores. *J. Phys. Chem. C* **2020**, *124*, 22568−22576.
(36) Grifoni, E.; Piccini, G. M.; Lercher, J. A.; Glezakou, V. A.; Rousseau, R.; Parrinello, M. Confinement Effects and Acid Strength in Zeolites. *Nat. Commun.* **2021**, *12*, No. 2630.
(37) DeLuca, M.; Hibbitts, D. Predicting Diffusion Barriers and Diffusivities of C6−C12 Methylbenzenes in MFI Zeolites. *Microporous Mesoporous Mater.* **2022**, *333*, No. 111705.
(38) Cnudde, P.; Demuynck, R.; Vandenbrande, S.; Waroquier, M.; Sastre, G.; Van Speybroeck, V. Light Olefin Diffusion during the MTO Process on H-SAPO-34: A Complex Interplay of Molecular Factors. *J. Am. Chem. Soc.* **2020**, *142*, 6007−6017.
(39) Cnudde, P.; Redekop, E. A.; Dai, W.; Porcaro, N. G.; Waroquier, M.; Bordiga, S.; Hunger, M.; Li, L.; Olsbye, U.; Van Speybroeck, V. Experimental and Theoretical Evidence for the Promotional Effect of Acid Sites on the Diffusion of Alkenes through Small-Pore Zeolites. *Angew. Chem., Int. Ed.* **2021**, *60*, 10016−10022.
(40) Bhan, A.; Joshi, Y. V.; Delgass, W. N.; Thomson, K. T. DFT Investigation of Alkoxide Formation from Olefms in H-ZSM-5. *J. Phys. Chem. B* **2003**, *107*, 10476−10487.
(41) Van Der Mynsbrugge, J.; Hemelsoet, K.; Vandichel, M.; Waroquier, M.; Van Speybroeck, V. Efficient Approach for the Computational Study of Alcohol and Nitrile Adsorption in H-ZSM-5. *J. Phys. Chem. C* **2012**, *116*, 5499−5508.
(42) Moors, S. L. C.; De Wispelaere, K.; Van Der Mynsbrugge, J.; Waroquier, M.; Van Speybroeck, V. Molecular Dynamics Kinetic Study on the Zeolite-Catalyzed Benzene Methylation in ZSM-5. *ACS Catal.* **2013**, *3*, 2556−2567.
(43) Yarulina, I.; De Wispelaere, K.; Bailleul, S.; Goetze, J.; Radersma, M.; Abou-Hamad, E.; Vollmer, I.; Goesten, M.; Mezari, B.; Hensen, E. J. M.; et al. Structure−Performance Descriptors and the Role of Lewis Acidity in the Methanol-to-Propylene Process. *Nat. Chem.* **2018**, *10*, 804−812.
(44) Kresse, G.; Hafner, J. *Ab initio* molecular-dynamics simulation of the liquid-metal−amorphous-semiconductor transition in germanium. *Phys. Rev. B* **1994**, *49*, 14251−14269.
(45) Kresse, G.; Furthmiiller, J. Efficiency of Ab-Initio Total Energy Calculations for Metals and Semiconductors Using a Plane-Wave Basis Set. *Comput. Mater. Sci.* **1996**, *6*, 15−50.
(46) Kresse, G.; Furthmüller, J. Efficient Iterative Schemes for *Ab Initio* Total-Energy Calculations Using a Plane-Wave Basis Set. *Phys. Rev. B* **1996**, *54*, 11169.
(47) Blöchl, P. E. Projector Augmented-Wave Method. *Phys. Rev. B* **1994**, *50*, 17953.
(48) Kresse, G.; Joubert, D. From Ultrasoft Pseudopotentials to the Projector Augmented-Wave Method. *Phys. Rev. B* **1999**, *59*, 1758.
(49) Perdew, J. P.; Burke, K.; Ernzerhof, M. Generalized Gradient Approximation Made Simple. *Phys. Rev. Lett.* **1996**, *77*, 3865−3868.
(50) Grimme, S.; Antony, J.; Ehrlich, S.; Krieg, H. A Consistent and Accurate Ab Initio Parametrization of Density Functional Dispersion Correction (DFT-D) for the 94 Elements H-Pu. *J. Chem. Phys.* **2010**, *132*, No. 154104.
(51) Heyden, A.; Bell, A. T.; Keil, F. J. Efficient Methods for Finding Transition States in Chemical Reactions: Comparison of Improved Dimer Method and Partitioned Rational Function Optimization Method. *J. Chem. Phys.* **2005**, *123*, No. 224101.
(52) Verstraelen, T.; Van Speybroeck, V.; Waroquier, M. ZEOBUILDER: A GUI Toolkit for the Construction of Complex Molecular Structures on the Nanoscale with Building Blocks. *J. Chem. Inf. Model.* **2008**, *48*, 1530−1541.
(53) Pulay, P. Convergence Acceleration of Iterative Sequences. the Case of Scf Iteration. *Chem. Phys. Lett.* **1980**, *73*, 393−398.
(54) Ghysels, A.; Van Neck, D.; Waroquier, M. Cartesian Formulation of the Mobile Block Hessian Approach to Vibrational Analysis in Partially Optimized Systems. *J. Chem. Phys.* **2007**, *127*, No. 164108.
(55) De Moor, B. A.; Ghysels, A.; Reyniers, M. F.; Van Speybroeck, V.; Waroquier, M.; Marin, G. B. Normal Mode Analysis in Zeolites: Toward an Efficient Calculation of Adsorption Entropies. *J. Chem. Theory Comput.* **2011**, *7*, 1090−1101.
(56) Zhi, Y.; Shi, H.; Mu, L.; Liu, Y.; Mei, D.; Camaioni, D. M.; Lercher, J. A. Dehydration Pathways of 1-Propanol on HZSM-5 in the Presence and Absence of Water. *J. Am. Chem. Soc.* **2015**, *137*, 15781−15794.
(57) Herrmann, S.; Iglesia, E. Elementary Steps in Acetone Condensation Reactions Catalyzed by Aluminosilicates with Diverse Void Structures. *J. Catal.* **2017**, *346*, 134−153.
(58) DeLuca, M.; Kravchenko, P.; Hoffman, A.; Hibbitts, D. Mechanism and Kinetics of Methylating C 6 −C 12 Methylbenzenes with Methanol and DME in H-MFI Zeolites. *ACS Catal.* **2019**, *9*, 6444−6460.

https://doi.org/10.1021/acscatal.2c03844
ACS Catal. 2022, 12, 14227−14242

(59) De Wispelaere, K.; Vanduyfhuys, L.; Van Speybroeck, V.Entropy Contributions to Transition State Modeling. In *Modelling and Simulation in the Science of Micro- and Meso-Porous Materials*; Elsevier Inc.: Amsterdam, 2018; pp 189−228.
(60) Ghysels, A.; Verstraelen, T.; Hemelsoet, K.; Waroquier, M.; Van Speybroeck, V. TAMkin: A Versatile Package for Vibrational Analysis and Chemical Kinetics. *J. Chem. Inf. Model.* **2010**, *50*, 1736−1750.
(61) Vandevondele, J.; Krack, M.; Mohamed, F.; Parrinello, M.; Chassaing, T.; Hutter, J. Quickstep: Fast and Accurate Density Functional Calculations Using a Mixed Gaussian and Plane Waves Approach. *Comput. Phys. Commun.* **2005**, *167*, 103−128.
(62) Kühne, T. D.; Iannuzzi, M.; Del Ben, M.; Rybkin, V. V.; Seewald, P.; Stein, F.; Laino, T.; Khaliullin, R. Z.; Schütt, O.; Schiffmann, F.; et al. CP2K: An Electronic Structure and Molecular Dynamics Software Package -Quickstep: Efficient and Accurate Electronic Structure Calculations. *J. Chem. Phys.* **2020**, *152*, No. 194103.
(63) Lippert, G.; Hutter, J.; Parrinello, M. A Hybrid Gaussian and Plane Wave Density Functional Scheme. *Mol. Phys.* **1997**, *92*, 477−487.
(64) Lippert, G.; Hutter, J.; Parrinello, M. The Gaussian and Augmented-Plane-Wave Density Functional Method for Ab Initio Molecular Dynamics Simulations. *Theor. Chem. Acc.* **1999**, *103*, 124−140.
(65) Yang, K.; Zheng, J.; Zhao, Y.; Truhlar, D. G. Tests of the RPBE, RevPBE, τ -HCTHhyb, ωb97X-D, and MOHLYP Density Functional Approximations and 29 Others against Representative Databases for Diverse Bond Energies and Barrier Heights in Catalysis. *J. Chem. Phys.* **2010**, *132*, No. 164117.
(66) Goedecker, S.; Teter, M.; Hutter, J. Separable Dual-Space Gaussian Pseudopotentials. *Phys. Rev. B* **1996**, *54*, 1703−1710.
(67) Nosé, S. A Molecular Dynamics Method for Simulations in the Canonical Ensemble. *Mol. Phys.* **1984**, *52*, 255−268.
(68) Martyna, G. J.; Klein, M. L.; Tuckerman, M. Nosé-Hoover Chains: The Canonical Ensemble via Continuous Dynamics. *J. Chem. Phys.* **1992**, *97*, 2635−2643.
(69) Martyna, G. J.; Tobias, D. J.; Klein, M. L. Constant Pressure Molecular Dynamics Algorithms. *J. Chem. Phys.* **1994**, *101*, 4177−4189.
(70) Torrie, G. M.; Valleau, J. P. Monte Carlo Free Energy Estimates Using Non-Boltzmann Sampling: Application to the Sub-Critical Lennard-Jones Fluid. *Chem. Phys. Lett.* **1974**, *28*, 578−581.
(71) Torrie, G. M.; Valleau, J. P. Monte Carlo Study of a Phase-Separating Liquid Mixture by Umbrella Sampling. *J. Chem. Phys.* **1977**, *66*, 1402−1408.
(72) Chodera, J. D.; Swope, W. C.; Pitera, J. W.; Seok, C.; Dill, K. A. Use of the Weighted Histogram Analysis Method for the Analysis of Simulated and Parallel Tempering Simulations. *J. Chem. Theory Comput.* **2007**, *3*, 26−41.
(73) Shirts, M. R.; Chodera, J. D. Statistically Optimal Analysis of Samples from Multiple Equilibrium States. *J. Chem. Phys.* **2008**, *129*, No. 124105.
(74) *ThermoLIB | Center for Molecular Modeling*. https://molmod.ugent.be/software/thermolib (accessed Nov 19, 2021).
(75) Cnudde, P.; De Wispelaere, K.; Van Der Mynsbrugge, J.; Waroquier, M.; Van Speybroeck, V. Effect of Temperature and Branching on the Nature and Stability of Alkene Cracking Intermediates in H-ZSM-5. *J. Catal.* **2017**, *345*, 53−69.
(76) Lee, C. K.; Chiang, A. S. T. Adsorption of Aromatic Compounds in Large MFI Zeolite Crystals. *J. Chem. Soc. Faraday Trans.* **1996**, *92*, 3445−3451.
(77) Schumacher, R.; Karge, H. G. Thermodynamics and Kinetics of Adsorption of Selected Monoalkylbenzenes in H-ZSM-5. *J. Phys. Chem. B* **1999**, *103*, 1477−1483.
(78) Piccini, G.; Alessio, M.; Sauer, J.; Zhi, Y.; Liu, Y.; Kolvenbach, R.; Jentys, A.; Lercher, J. A. Accurate Adsorption Thermodynamics of Small Alkanes in Zeolites. Ab Initio Theory and Experiment for H-Chabazite. *J. Phys. Chem. C* **2015**, *119*, 6128−6137.
(79) Amsler, J.; Plessow, P. N.; Studt, F.; Bucko, T. Anharmonic Correction to Adsorption Free Energy from DFT-Based MD Using Thermodynamic Integration. *J. Chem. Theory Comput.* **2021**, *17*, 1155−1169.
(80) Galimberti, D. R.; Sauer, J. Chemically Accurate Vibrational Free Energies of Adsorption from Density Functional Theory Molecular Dynamics: Alkanes in Zeolites. *J. Chem. Theory Comput.* **2021**, *17*, 5849−5862.
(81) Eckstein, S.; Hintermeier, P. H.; Zhao, R.; Baráth, E.; Shi, H.; Liu, Y.; Lercher, J. A. Influence of Hydronium Ions in Zeolites on Sorption. *Angew. Chem., Int. Ed.* **2019**, *58*, 3450−3455.
(82) Vjunov, A.; Wang, M.; Govind, N.; Huthwelker, T.; Shi, H.; Mei, D.; Fulton, J. L.; Lercher, J. A. Tracking the Chemical Transformations at the Brønsted Acid Site upon Water-Induced Deprotonation in a Zeolite Pore. *Chem. Mater.* **2017**, *29*, 9030−9042.
(83) Fu, D.; Erik Maris, J. J.; Stanciakova, K.; Nikolopoulos, N.; van der Heijden, O.; B Mandemaker, L. D.; Siemons, M. E.; Salas Pastene, D.; Kapitein, L. C.; Rabouw, F. T.; et al. Unravelling Channel Structure−Diffusivity Relationships in Zeolite ZSM-5 at the Single-Molecule Level. *Angew. Chem., Int. Ed.* **2022**, *61*, No. e202114388.
(84) Pérez de Alba Ortíz, A.; Tiwari, A.; Puthenkalathil, R. C.; Ensing, B. Advances in Enhanced Sampling along Adaptive Paths of Collective Variables. *J. Chem. Phys.* **2018**, *149*, No. 072320.
(85) Grifoni, E.; Piccini, G. M.; Parrinello, M. Microscopic Description of Acid−Base Equilibrium. *Proc. Natl. Acad. Sci. U.S.A.* **2019**, *116*, 4054−4057.

https://doi.org/10.1021/acscatal.2c03844
ACS Catal. 2022, 12, 14227−14242